NANO · MICRO small
www.small-journal.com

An Unbalanced Battle in Excellence: Revealing Effect of Ni/Co Occupancy on Water Splitting and Oxygen Reduction Reactions in Triple-Conducting Oxides for Protonic Ceramic Electrochemical Cells

Wei Tang, Hanping Ding, Wenjuan Bian, Clarita Y. Regalado Vera, Joshua Y. Gomez, Yanhao Dong, Ju Li, Wei Wu, WeiWei Fan, Meng Zhou, Colin Gore, Bryan M. Blackburn, Hongmei Luo,* and Dong Ding**

Porous electrodes that conduct electrons, protons, and oxygen ions with dramatically expanded catalytic active sites can replace conventional electrodes with sluggish kinetics in protonic ceramic electrochemical cells. In this work, a strategy is utilized to promote triple conduction by facilitating proton conduction in praseodymium cobaltite perovskite through engineering non-equivalent B-site Ni/Co occupancy. Surface infrared spectroscopy is used to study the dehydration behavior, which proves the existence of protons in the perovskite lattice. The proton mobility and proton stability are investigated by hydrogen/deuterium (H/D) isotope exchange and temperature-programmed desorption. It is observed that the increased nickel replacement on the B-site has a positive impact on proton defect stability, catalytic activity, and electrochemical performance. This doping strategy is demonstrated to be a promising pathway to increase catalytic activity toward the oxygen reduction and water splitting reactions. The chosen $PrNi_{0.7}Co_{0.3}O_{3-\delta}$ oxygen electrode demonstrates excellent full-cell performance with high electrolysis current density of –1.48 A cm^{-2} at 1.3 V and a peak fuel-cell power density of 0.95 W cm^{-2} at 600 °C and also enables lower-temperature operations down to 350 °C, and superior long-term durability.

1. Introduction

To accelerate decarbonization, increasing the generation and storage capacities of renewable energies can significantly reduce the dependency on fossil fuels.[1] Converting intermittent renewable electricity and heat into high specific energy density of hydrogen via high-temperature steam electrolysis could be a promising approach to store renewable energies and achieve zero carbon emission. The electrochemical solid oxide cell is an all-ceramic device that can efficiently produce hydrogen from clean electricity in the electrolysis mode, then convert it back into fuel cell mode for peak shaving and seasonal energy storage.[2] In particular, protonic ceramic electrochemical cells (PCECs) that use proton conductors as electrolyte are an emerging technology that has clear technical advantages: lower activation energy, reduced operating temperature, no fuel separation/drying, cheaper system manufacturing, and lower operation cost.[3] Due to the high ionic conductivity, PCECs can have lower resistive losses in intermediate-to-low temperature electrochemical cells than oxygen-conducting cells since electricity accounts for the overall cost of more than 50%.

Although PCECs have many advantages, the development of efficient and durable PCECs is hindered by the poor activity

W. Tang, H. Ding, W. Bian, C. Y. Regalado Vera, J. Y. Gomez, W. Wu, D. Ding
Energy and Environment Science & Technology
Idaho National Laboratory
Idaho Falls, ID 83415, USA
E-mail: hanping.ding@inl.gov; dong.ding@inl.gov
W. Tang, C. Y. Regalado Vera, M. Zhou, H. Luo
Department of Chemical and Materials Engineering
New Mexico State University
Las Cruces, NM 88003, USA
E-mail: hluo@nmsu.edu
The ORCID identification number(s) for the author(s) of this article can be found under https://doi.org/10.1002/smll.202201953.
Y. Dong, J. Li, W. Fan
Department of Nuclear Science and Engineering
Massachusetts Institute of Technology
Cambridge, MA 02139, USA
J. Li
Department of Materials Science and Engineering
Massachusetts Institute of Technology
Cambridge, MA 02139, USA
C. Gore, B. M. Blackburn
Redox Power Systems, LLC
Beltsville, MD 20705, USA

DOI: 10.1002/smll.202201953

and stability of the oxygen electrode where water oxidation reaction (WOR) and oxygen reduction reaction (ORR) take place in electrolysis or fuel-cell mode.[4] These reactions contribute to a large fraction of cell resistance, often termed polarization resistance.[5] Because the reactions are strictly confined to the limited triple-phase boundaries where ion, electron, and gas meet, the use of triple-conductor oxides (TCOs) as oxygen/steam electrodes in PCECs is a promising method to greatly expand the number of catalytic sites and potentially address this issue.[6] TCOs are ceramics that conduct protons, oxygen ions, and electrons simultaneously. The mobility of multiple charge carriers can expand reaction site density over the entire electrode surface when exposed to humid conditions, resulting in higher cell performance by reducing polarization resistance.[7] Some examples include the widely studied double-layered perovskite like $PrBa_{0.5}Sr_{0.5}Co_{1.5}Fe_{0.5}O_{5+\delta}$ (PBSCF), and our recently reported A-site deficient double-layered perovskite $(PrBa_{0.8}Ca_{0.2})_{0.95}Co_2O_{5+\delta}$ (PBCC95).[8] Recently, Kim has evaluated the proton diffusion coefficient of PBSCF at 550 °C to be 1.04×10^{-6} cm^2 s^{-1}, which is higher than the oxygen diffusion coefficient of most typical mixed oxygen ionic and electronic conductors.[6] The proton surface exchange coefficient of PBSCF is also measured to be 2.60×10^{-7} cm s^{-1}. The study of PBCC95 and its parent material of stoichiometric $PrBa_{0.8}Ca_{0.2}Co_2O_{5+\delta}$ shows that introducing A-site deficiency can enhance its catalytic activity with increased oxygen vacancy concentration and increased ion conduction.[8a] Another promising type of TCO that has been developed recently is the transition metal doped proton conductor oxide. This includes Co and Fe co-doped $BaCo_{0.4}Fe_{0.4}Zr_{0.1}Y_{0.1}O_{3-\delta}$ (BCFZY),[9] which exhibits good performance working in both fuel-cell mode and electrolysis mode for PCECs. However, these alkaline-earth-containing electrodes have a common instability issue in steam or carbon dioxide, which raises concern about the operation stability in realistic conditions, where a high steam concentration (e.g., >50% H_2O) is needed.[10] Therefore, developing an electrode composition with less- or non-alkaline earth elements is critical.

A rationally designed alkaline-earth-element-free TCO $PrNi_{0.5}Co_{0.5}O_{3-\delta}$ by doping 50% Ni in $PrCoO_3$ was recently reported as the oxygen electrode exhibiting high activity toward WOR and ORR in reversible operation conditions.[11] The mechanism study via density function theory calculation indicated that the Ni dopant in the B-sites can decrease the protonic migration energy and increase the proton conductivity. However, the underlying mechanism, especially from a quantitative perspective, remains elusive. In this work, we aim to disclose the intriguing relationship between electrode composition and proton conduction behavior and subsequent reaction kinetics by a series of electrochemical characterizations, confirmation of proton defects, and electrode performance evaluation. Multiple techniques are deployed to study the origin of proton conduction and reaction activity such as water temperature-programmed desorption (TPD) for studying the dissociated proton defects near different lattice oxygen sites, isotope exchange experiment under a humid atmosphere to prove proton uptake property, and the Fourier-transform infrared spectroscopy (FTIR) to observe active hydroxyl species on the surface.

2. Results and Discussion

The $PrNi_xCo_{1-x}O_{3-\delta}$ (x = 0.1, 0.3, 0.5, 0.7, and 0.9, noted as PNC19, PNC37, PNC55, PNC73, and PNC91, respectively) series electrode powders were synthesized by the glycine-citrate combustion method as illustrated in Figure S1, Supporting Information. After calcined at 1000 °C in air, inductively coupled plasma atomic emission spectroscopy (ICP-AES) analysis was characterized which shows that the actual compositions of all the PNC samples are close to their nominal values, as shown in Table S1, Supporting Information. X-ray photoelectron spectroscopy (XPS) was carried out to measure the chemical status of PNC55 and PNC73 after Ni doping. In general, all cations in PNC55 and PNC73 show mixed valences, and dominant valences are identified as Pr^{3+}, Ni^{2+}, and Co^{3+} as shown in Figure S2a–d, Supporting Information. The phase purity and crystalline structure were examined by powder X-ray diffraction (XRD). As shown in **Figure 1**a,b, the PNC electrodes with Ni ratio from 0.1 to 0.7 show pure phase with XRD patterns matching well with single orthorhombic perovskite structure indexed to be *Pbnm* space group. For PNC91 with the highest Ni content, it shows the co-existence of orthorhombic and rhombohedral phases relating to the space group of *Pbnm* and *R-3c*, respectively.[12] Minor impurities of NiO and Pr_2O_3 are also detected. A pure phase for the PNC with high Ni content can be difficult to achieve due to the instability of Ni^{3+} in the relatively low oxygen partial pressure of air.[13] The crystal structure of orthorhombic PNC is schematically shown in Figure 1c. The Co and Ni ions (B-site cations) are distributed at the center of the BO_6 octahedra coordination. The trivalent Pr atoms locate at the A-site, surrounded by tiled octahedra. It was confirmed that the Ni doping at B sites has a mild effect on changing the unit-cell parameters. In the magnified pattern zone (32–35°), the (121) plane peak shifted to a lower angle when the Ni doping level was gradually increased. The lattice increase or unit cell volume expansion should be attributed to the larger ionic radius of Ni^{2+} (69 pm) than Co^{3+} ion (61 pm) at B-site.[14] The larger molar volume (lattice constants) may be beneficial for the formation and mobility of protonic charge carriers in perovskite-related structures.[15] The thermal expansion behaviors of PNC series material and $BaCe_{0.4}Zr_{0.4}Y_{0.1}Yb_{0.1}O_3$ (BCZYYb4411) electrolyte were tested from room temperature to 1000 °C as shown in Figure S3a, Supporting Information. All of the PNC series materials show higher thermal expansion than the BCZYYb4411 electrolyte. For example, the calculated thermal expansion coefficient (TEC) from 100 to 1000 °C are 22.3×10^{-6}, 20.3×10^{-6}, 18.8×10^{-6}, 15.9×10^{-6}, and 14.5×10^{-6} K^{-1}, for PNC19, PNC37, PNC55, PNC73, and PNC91, respectively. With higher B-site Ni ratios, the TEC shows a decreasing trend closer to BCZYYb4411 (TEC of 10.7×10^{-6} K^{-1}) as shown in Figure S3b, Supporting Information. The high TEC mismatch may lead to the weak bonding of oxygen electrodes to electrolytes and increase the risk of delamination.[16] Hence, the higher B-site Ni doping can effectively alleviate the TEC mismatch for better compatibility with the proton conducting oxide electrolyte.

When the PNC is integrated into symmetric cells, the electrode polarization resistance (R_p) can be measured to study the catalytic activity toward ORR and WOR, respectively. **Figure 2**a

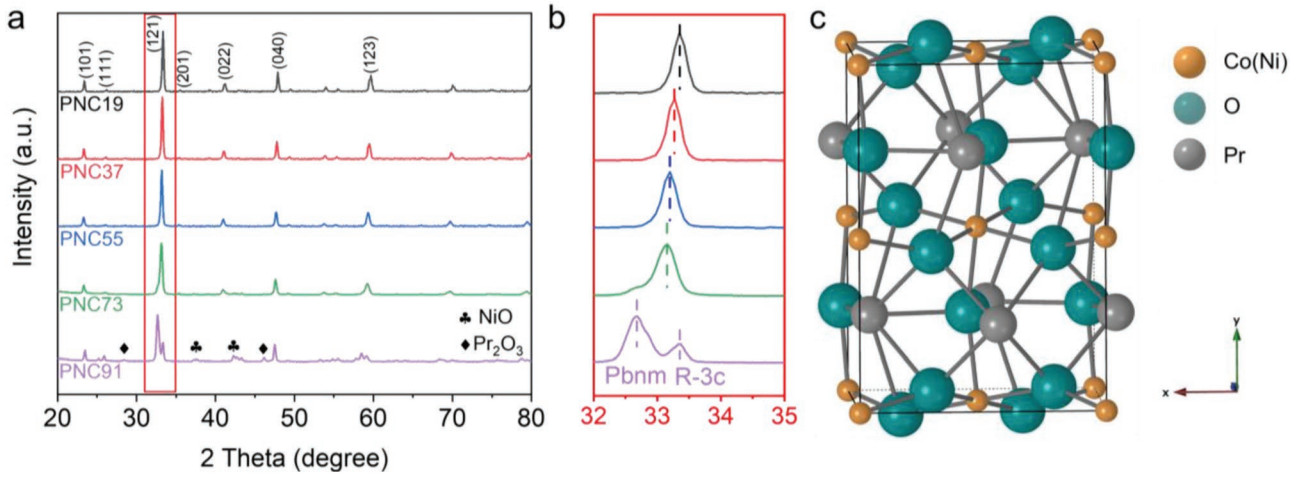

Figure 1. The phase structure of the synthesized PNC series electrode materials. a) X-ray diffraction patterns collected at room temperature; b) Magnified area of the patterns between 32° and 35°; and c) Schematic diagram of the ideal crystal structure.

displays the comparison of the polarization resistances for each composition tested at open-circuit voltage (OCV) condition with a four-probe measurement (described in Figure S4a, Supporting Information). It can be clearly seen that the PNC73 exhibited the smallest resistance at 600 °C (e.g., the R_p of PNC73 is smaller than PNC19, PNC37, PNC55, and PNC91 by 73.4%, 64.3%, 32.0%, and 49.8%, respectively). Furthermore, the PNC73 also shows the smaller R_p at lower temperatures of 400 to 550 °C. The activation energies are calculated using the following equation:

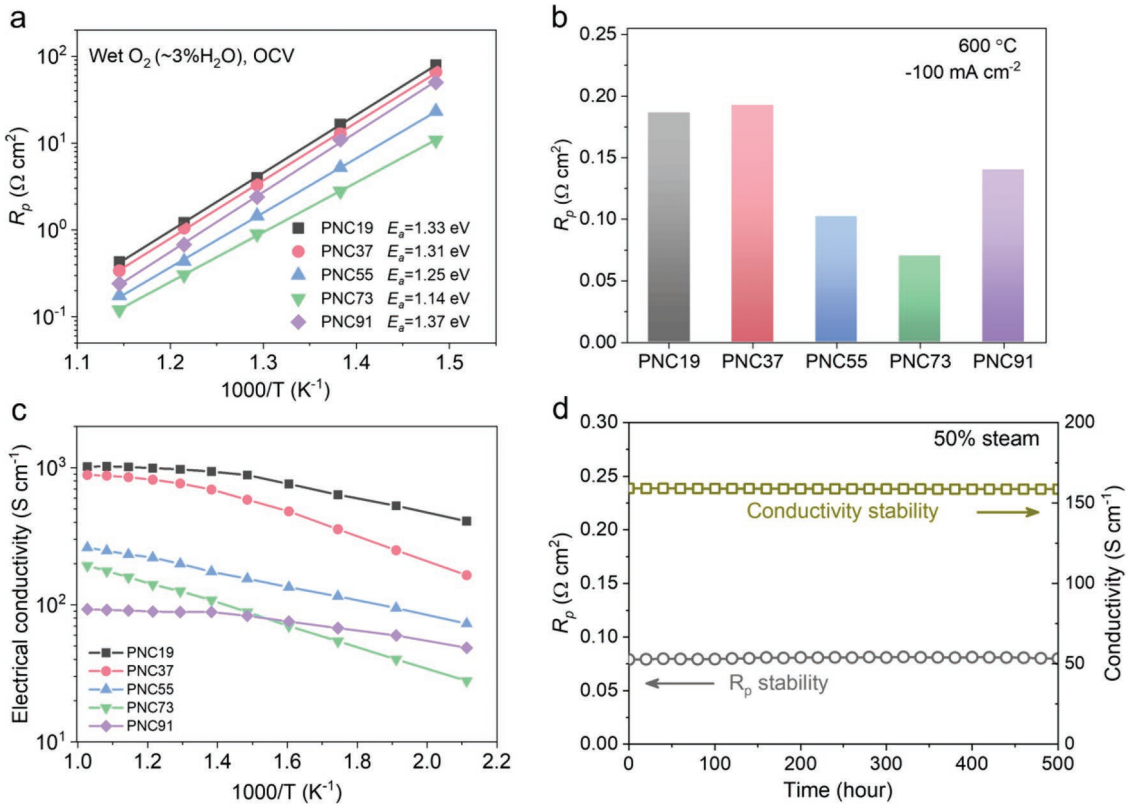

Figure 2. Electrical and electrochemical property characterizations of PNC electrodes. a) Arrhenius plot of electrode polarization resistances measured from symmetric cells under open circuit and wet oxygen conditions (≈3% H_2O); b) Polarization resistance comparison with an applied current of –100 mA cm^{-2} measured at 600 °C with the three-electrode configuration; c) Electrical conductivity as a function of temperature from 200 to 700 °C, measured by direct-current four-probe method under wet oxygen (≈3% H_2O); d) The durability of the conductivity and polarization resistance of the PNC73 electrode in the practical electrolysis operation condition: conductivity stability in humidified oxygen (≈50% H_2O) and R_p stability in humidified oxygen (≈50% H_2O) testing at 600 °C and –100 mA cm^{-2}.

$$R_p = R_p^0 \exp\left(E_a / k_B T\right) \quad (1)$$

where k_B is the Boltzmann constant 1.38×10^{-23} J K^{-1}; E_a is the activation energy; T is the temperature.

The activation energy shows the order 1.14 eV (PNC73) < 1.25 eV (PNC55) < 1.31 eV (PNC37) < 1.33 eV (PNC19) < 1.37 eV (PNC91). PNC73 exhibit the smallest E_a among the PNC series, which is similar to recently developed advanced oxygen electrodes, for example, PBSCF with optimized structure (≈1.19 eV), A-site deficient BCFZY (≈1.17 eV), and PBCC95 (≈1.12 eV).[8a,17] Therefore, from an electrical/electrochemical performance perspective, the results indicate that the PNC73 could be the optimal composition, while some further characterizations are needed to demonstrate the proton conductivity and catalytic activity.

To study the effect of the applied electrolysis current density on R_p and to avoid the interruption of the counter-reaction, the impedance spectra of the symmetric cell with the PNC73 electrode were measured under a three-electrode configuration as illustrated in Figure S4b, Supporting Information. Different bias currents were applied to simulate the operating condition in the electrolysis mode. As can be observed in Figure S5, Supporting Information, the R_p shows an obvious decreasing trend when the applied current density gradually increased from −10 to −200 mA cm^{-2}, indicating the enhanced electrode reaction kinetics in the applied electrolysis current condition.[8a] The R_p at 600 °C with a current density of −100 mA cm^{-2} was compared to other PNC compositions as shown in Figure 2b. PNC73 exhibits the smallest R_p (≈0.07 Ω cm^2) among the PNC series materials, indicating that PNC73 has the advantage of high catalytic activity in the electrolysis mode.

To evaluate the properties of the PNC electrodes for the PCEC application, the total electrical conductivity of the PNC series oxygen electrodes was measured as shown in Figure 2c. Dense PNC bars were fabricated by pressing 1 g of PNC powder with a 4 mm × 20 mm die and then fired at 1250 °C for 5 h. The sintered PNC55 bar was used as an example to characterize the microstructure by scanning electron microscope (SEM) (Figure S6a,b, Supporting Information), which shows relatively dense morphology for the conductivity measurement. For perovskite structured oxygen electrode materials, the electronic conductivity takes the dominance over ionic conductivity, and it is assumed that the transition metals (TM) cations in B-site can perform a valence change and create TM^{4+}/TM^{3+} or TM^{3+}/TM^{2+} couples, which act as hopping sites for electrons (n type)/holes (p type).[18] The BO_6 octahedra build up a network throughout the perovskite structure for electronic conduction. Therefore, PNC series material with different Ni/Co doping ratios in B-site will largely affect their electrical conductivity. Even so, the PNC series material shows a similar trend for the tested temperature range. First, the conductivity of all the PNC compositions is higher than 100 S cm^{-1} at the typical operating temperature range, which is favorable for the oxygen electrode.[19] Second, PNC19 and PNC37 with higher Co/Ni ratios exhibit higher conductivity compared to the other PNC compositions with higher Ni ratios in B-site. However, we cannot naturedly refer to the higher conductivity as a better electrochemical performance because the PNC series material has enough electrical conductivity and it will not be the limiting step for the electrocatalytic process. Third, elevated temperatures increased the conductivity for all compositions in the entire temperature range (200 to 700 °C), which is regarded as a semiconductor behavior. For example, when the temperature was increased from 200 to 450 °C, a significant increase in conductivity was observed, for example, 165 to 651 S cm^{-1} for PNC37, and 407 to 938 S cm^{-1} for PNC19, respectively. However, their conductivity gradually leveled off, indicating the possible transition of semiconducting to metallic conduction. This electrical conductivity transition behavior is also reported by other oxygen electrodes. For example, double perovskite $PrBaCo_2O_{5+\delta}$ and the Ni-doped $PrBaCo_{2-x}Ni_xO_{5+\delta}$ show semiconductor conductivity when the temperature is below 250 °C, and a metallic transition behavior can be observed at higher temperatures.[20] Ruddlesden–Popper (R–P) structured $Ln_{1.2}Sr_{0.8}NiO_4$ (Ln = La and Pr) also shows the semiconductor to metal transition behavior at around 700 °C.[21] This phenomenon could be attributed to the excessive oxygen loss from the lattice. The oxygen vacancy at high temperatures can randomly trap electrons, which reduces its carrier mobility.[22] Similarly, the conductivities of PNC55 and PNC73 electrodes show the same trend with smaller conductivity. Finally, the PNC91 showed an irregular trend due to the complex compositions after sintering, including Pr_2NiO_4, NiO, and Pr_2O_3, as indicated in XRD spectra (Figure S7, Supporting Information).

Chemical stability and electrochemical stability of PNC73 at 600 °C were evaluated in a symmetrical cell with humidified oxygen (≈50% H_2O) by monitoring conductivity and R_p (at −100 mA cm^{-2}) as a function of time, respectively, as shown in Figure 2d. Beforehand, the PNC73 conductivity at low steam atmosphere (≈3% H_2O) and high steam atmosphere (≈50% H_2O) was compared for different temperatures as shown in Figure S8a, Supporting Information. These results show that similar conductivity can be achieved under these two testing conditions. Then, the conductivity was collected every 5 h under 50% steam at 600 °C. The aim of the chemical stability experiment was to observe a possible reduction in bulk conductivity from the generated less conductive phase by the chemical reaction between PNC and steam at operating temperature. No degradation in PNC73 conductivity was observed after 500 h. XRD was measured after the 500 h test (Figure S8b, Supporting Information), which shows the pure phase of PNC73 that confirmed the excellent chemical stability under 50% steam atmosphere condition. The electrochemical stability was measured using a symmetrical cell with PNC73 as a working electrode under the 50% steam atmosphere condition with an applied current of −100 mA cm^{-2}. R_p of PNC73 was collected every 5 h and no observable degradation was observed. Overall, PNC73 shows good chemical and electrochemical stability over 500 h.

As a representative electrode, the morphology, lattice structure, and element distribution of the PNC73 electrode are characterized by an electron microscope. As shown in **Figure 3**a (Transmission Electron Microscopes, TEM) and Figure S9a,b, Supporting Information, (SEM), PNC73 powder shows net-like morphology with particle sizes of about 100–200 nm. Good crystallization with an interplanar lattice distance of 0.382 nm was identified (Figure 3b), which fits well with the d spacing of the (101) plane and is consistent with the XRD result. The

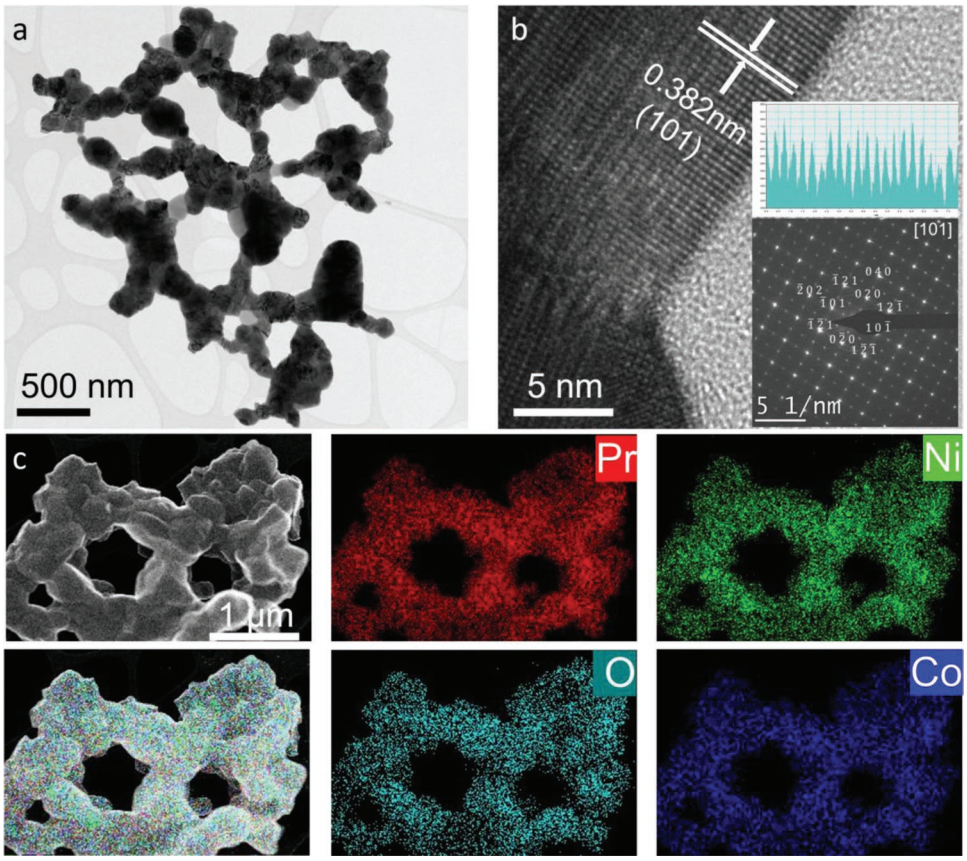

Figure 3. Morphology and lattice structure of the PNC73 electrode. a) TEM image of synthesized fresh powders; b) High-resolution TEM image of lattice edge area to highlight lattice fringe; (inset) lattice measurement and selected area electron diffraction (SEAD) pattern corresponding to [101] zone axes; and c) EDX mapping of PNC73 to show uniform elements distribution of cations and oxygen.

distance of the spots was measured and calculated by the Gatan Microscopy software as shown in the inset figure, which demonstrates the orderliness and uniformity of the lattice plane. The diffraction pattern on a single particle exhibited a single crystal structure corresponding to the [101] zone axis, consistent with the XRD pattern. The uniform distribution of the cations and oxygen was confirmed by energy-dispersive X-ray spectroscopy (EDX) mapping of a single particle (Figure 3c).

Several techniques were used to confirm proton conductivity within the optimal composition of PNC73 and to study its proton behavior. First, the PNC73 powder was studied by in situ FTIR to observe the chemisorbed water concentration evolution on the surface during the hydration and dehydration process at the temperature range of 100–600 °C. The rationally designed procedure is to monitor −OH group change on the surface during the dehydration process: 1) first, PNC73 was hydrated at 500 °C for 2 h with 3% steam in the air; 2) then, the temperature was gradually decreased to 100 °C with a continuous flow of wet air; 3) after switching to dry Ar and flushing for 1 h, the baseline was collected; and 4) dehydration was carried out in dry Ar and subsequently the FTIR spectra were collected every 100 °C from 100 to 600 °C with the flow of dry Ar. All the collected data were plotted as a differential spectrum with the spectra at 100 °C used as the baseline (**Figure 4**a). The strong and broad peak between 3000 and 3500 cm^{-1} can be ascribed to the −OH stretching band.[23] For PNC73, the dehydration process can be studied via observation of a decreasing −OH group signal in the FTIR spectra. The negative −OH stretching band peak indicates a loss of the −OH group. The dehydration process during heating is schematically illustrated in Figure 4b. The higher peak intensity and the larger integrated peak indicate more desorption of chemisorbed water or protons. The negative peak intensity increased rapidly before 400 °C and then slowly after 400 °C, which indicates a large portion of the protons are dehydrated at temperatures lower than 400 °C, while there are still few surface-stabilized protons at 600 °C. Therefore, the observed signal change for protons on the surface demonstrates that the PNC73 electrode has been hydrated and possesses a certain concentration of proton defects to enable proton conductivity for the electrode reactions.

To verify proton mobility, heavy water (deuterium oxide, D_2O) was used in an isotope exchange experiment to observe the hydrogen/deuterium (H/D) ion interdiffusion. The hydrated PNC73 was exposed to 3% heavy water for 24 h. After switching to dry Ar gas, the water species (H_2O, HDO, and D_2O) signal was monitored with a mass spectrometer (MS) in a heating process as shown in Figure 4c. There are three distinct peaks for D_2O located at around 204, 335, and 468 °C. For HDO, there are only two weak peaks located at the 176 °C and middle-temperature range (≈332 °C). Both HDO and

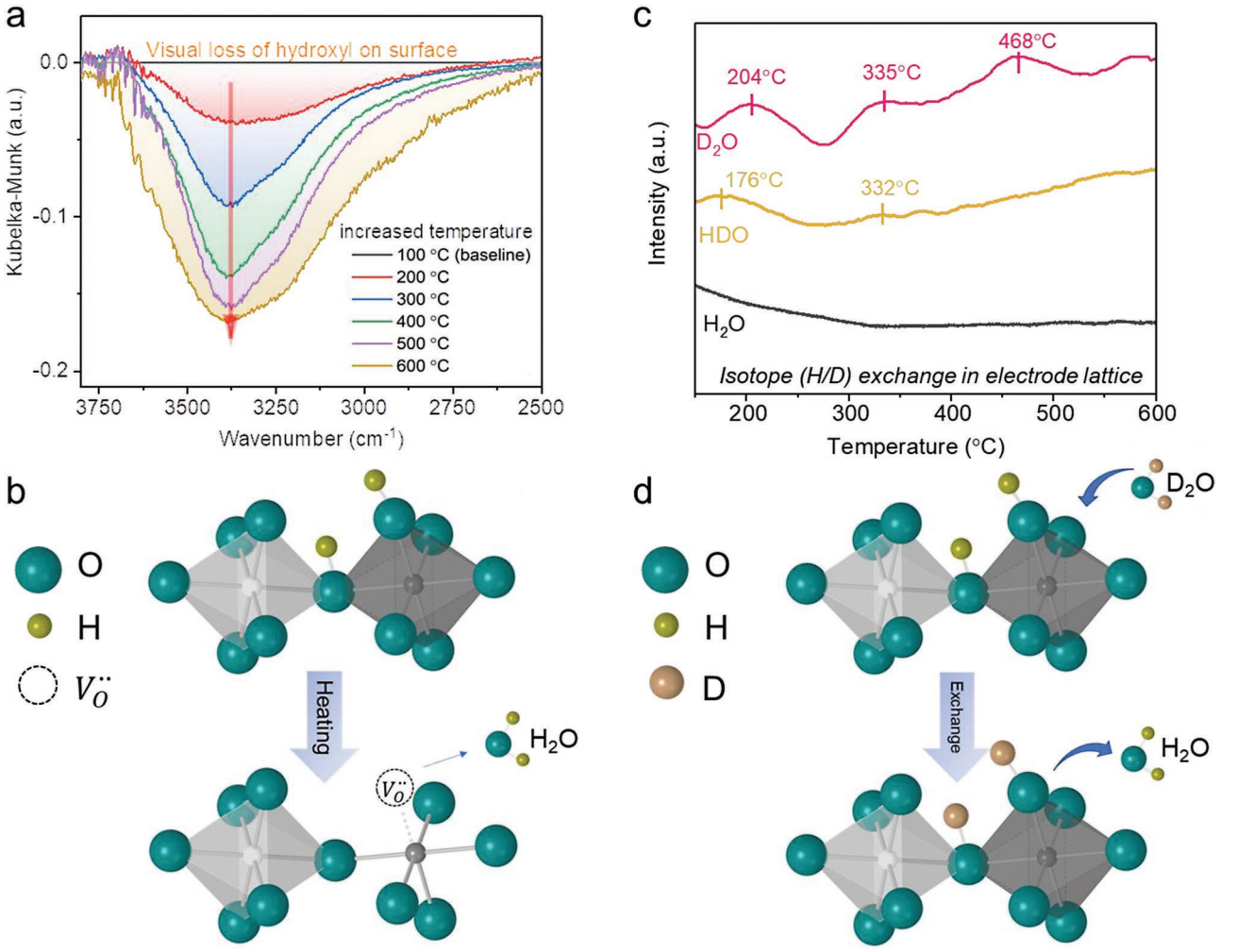

Figure 4. Characteristic proton defect confirmation by various techniques for PNC73 electrode. a) In situ FTIR spectra in dry argon at different temperatures (100–600 °C); b) The dehydration movement within the bulk during heating treatment; c) Water species (H_2O, HDO, and D_2O) desorption signals measured from 150–600 °C after isotope H/D exchange at 200 °C for 24 h; d) The schematic of H/D isotope exchange process on the proton defect site.

D_2O signals are relating to the chemisorbed $OD_O^{\cdot}$ in PNC73 lattice, which proved the successful isotope exchange from heavy water. There is no discernible H_2O signal after the H/D exchange process, indicating the non-existence or low concentration of $OH_O^{\cdot}$ in the PNC73 lattice. In contrast, the controlled experiment was carried out to show the H_2O signal without an isotope exchange process as shown in Figure S10, Supporting Information. PNC73 was hydrated in H_2O for 24 h but not exchanged with D_2O in the next step. After cooling down and flushed with dry Ar gas, the H_2O signal was collected similarly. There are also three peaks, which are located at around 218, 361, and 495 °C, similar to the D_2O result after the H/D exchange. Therefore, it is proved that most of $OH_O^{\cdot}$ proton species has been replaced by $OD_O^{\cdot}$ after 24 h H/D exchange at 200 °C. Figure 4d is a schematic illustration to show how deuterium gradually replaces a proton in the proton-defect position and forms a new deuterium defect. This process can be described as the $OD_O^{\cdot}$ and $OH_O^{\cdot}$ proton species dynamically exchanged on the hydrated PNC73 surface and the $OD_O^{\cdot}$ further move into the lattice for proton transportation.

To distinguish the catalytic activity toward the oxygen reduction and water splitting reactions for the different electrode compositions, the O_2-TPD and H_2O-TPD techniques were employed to examine the surface and lattice oxygen or hydroxyl species to explain the observed activity or conductivity. As shown in **Figure 5**a, the spectra show oxygen desorption peaks during the heating process, which correspond to different oxygen species on the electrode surface or lattice. These oxygen species are closely involved in electrochemical reactions. For $PrCoO_3$ and higher Co-containing PNC materials (PNC19 and PNC37), there are two distinct oxygen desorption peaks at temperatures lower than 400 °C (shown in Figure 5a and Figure S11, Supporting Information), which indicates oxygen dissociation from two different oxygen sites (O1 and O2) in the crystal lattice. This result is consistent with the $PrCoO_3$ crystal structure in Springer database, which shows two oxygen atom coordinates O1 (x = 0.1984, y = 0.0506, z = 0.3043) and O2 (x = 0.5328, y = 1/4, z = 0.6005).[24] When the Co content is decreased to 50% or lower, for example, PNC55, PNC73, and PNC91, there is another oxygen peak between 400 and 500 °C, suggesting a new

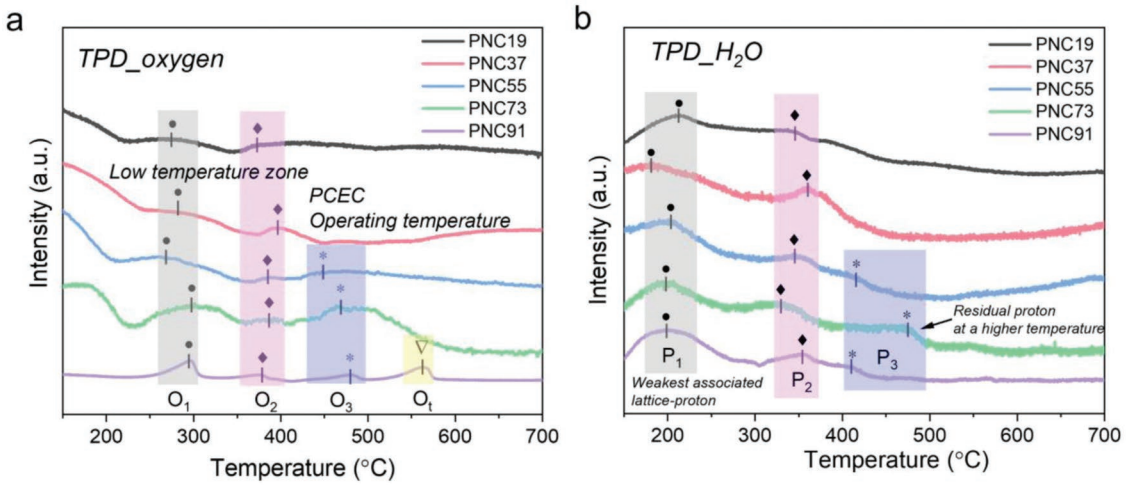

Figure 5. Lattice oxygen and chemisorbed proton stabilities of PNC electrodes. a) The O_2-TPD experiments for detecting oxygen defect species by in situ analyzing the product from the surface via mass spectroscopy. Peaks O1 and O2 located at 250–320 °C and 360–410 °C are related to two different oxygen positions with different bonding energies with cations. Peak O3 located at 440–500 °C relating to the new emerging peak due to the Ni doping. Peak Ot for PNC91 at around 562 °C relates to the oxygen loss after the crystal structure transforms from orthorhombic to rhombohedral due to the high Ni content. b) The H_2O-TPD profiles of PNC electrodes for scanning the possible proton defects involved in the water splitting reaction. Peaks P1, P2, and P3 located at 170–230, 320–370, and 400–500 °C are related to different —OH groups absorbed at different oxygen deficiency positions with different bonding energies. For each composition, the proton positions are the same as oxygen positions except the crystal structure change of PNC91.

oxygen site (O3) near a Ni cation, that is, Ni—O—Co from the original Co—O—Co site. For PNC91 with the highest Ni ratio in the series, there are four oxygen desorption peaks in total. Except for the O1, O2, and O3 in the original crystal structure, a new peak (Ot) around 563 °C appeared, relating to the oxygen site after phase change from orthorhombic to rhombohedral and the crystal lattice parameters a and b to a_{rhomb}.[12,25] With increased Ni doping level, PNC showed a broader temperature window for oxygen adsorption/desorption and higher desorption temperature, indicating stronger bonds between the surface and the adsorbate.

As an oxygen electrode working in PCEC, the proton conductivity plays a critical role in promoting the reaction kinetics. Proton conductivity is an essential criterion for a high-performance electrode. To enable this proton conduction, the abundance of oxygen vacancies by Ni replacement can facilitate the hydration reaction to introduce a proton charge carrier in the lattice. Therefore, identification of the proton conduction behavior can give some fundamental information on the existence and evolution of the proton defects in the material. In this work, the H_2O-TPD was first used to study proton desorption of the PNC electrodes with dependence on the Ni/Co ratio. The samples were hydrated at 500 °C first and then cooled down to 100 °C for flushing with dry Ar to purge and remove possible physisorbed water residue in the testing apparatus and PNC electrode powder surface. After this purging treatment, the water signals detected by mass spectroscopy during the heating process to 700 °C can be considered as coming from the proton defects dissociated from the surface or lattice. As shown in Figure 5b, the major water peaks corresponding to proton dehydration are similar to the peaks from the oxygen-TPD results, which indicates that the oxygen sites have been hydrated to form the proton defects accordingly. This hydration/dehydration process can be written as below:

$$H_2O + V_O^{\cdot\cdot} + O_O^{\times} \leftrightarrow 2OH_O^{\cdot} \quad (2)$$

Compared to PNC19 and PNC37 showing two major dehydration peaks, PNC55, PNC73, and PNC91 exhibited three peaks, which might be related to the protons located at new oxygen sites (O3) introduced by the Ni doping as discussed above. Among all PNC electrode compositions, PNC73 demonstrated the highest H_2O desorption temperature at around 480 °C. The higher dehydration temperature indicates higher bonding energy of PNC73 to the proton, or that the proton defect is more stable in the oxygen site. This suggests that Ni doping favors the stabilization of protons within the lattice to ensure reasonable proton conductivity. Based on the kinetics dynamics, proton conductivity can be mainly determined by two factors: the proton diffusivity D_{proton}, and the proton concentration c_{proton}, according to the following equation:[3a,26]

$$\sigma_{proton} = \frac{F^2 D_{proton} c_{proton}}{RT} \quad (3)$$

Therefore, PNC73 would have a higher c_{proton} at higher temperatures compared to other compositions, which is proportional to the proton conductivity. In other words, PNC73 has stabilized protons at the operation temperature increasing the proton transport and promoting the electrode catalytic reaction.

To further evaluate the feasibility of PNC in the cell system, electrodes were integrated into PCEC button cells to evaluate their electrochemical performance. The BCZYYb4411 was used as the protonic ceramic electrolyte. The fuel cell and water electrolysis mode of operation were measured with respective gas conditions. The performance in fuel cell mode was collected under wet H_2 (3% steam) on the fuel side and pure oxygen on the oxygen side. First, the OCV was measured, and all cells showed an average of 1.04 V at 600 °C (**Figure 6**a), which

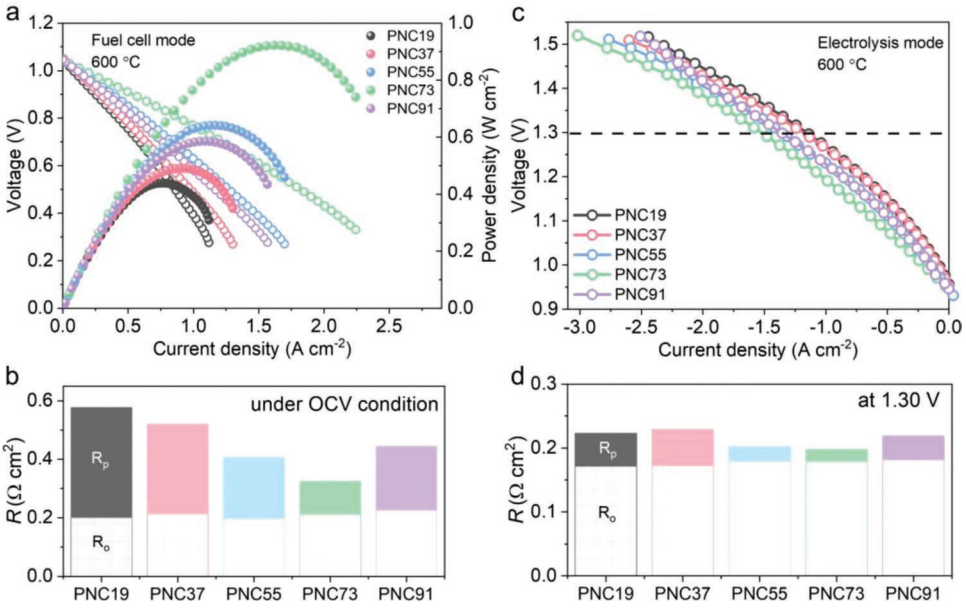

Figure 6. Electrochemical performances of PNC series electrodes at 600 °C. a) Current–voltage (*I–V*) and current–power density (*I–P*) curves tested in fuel cell mode with wet H_2 (3% steam) fed into the fuel side and pure oxygen fed into the oxygen side; b) Total resistance comparison of PNC tested under OCV condition with R_{ohm} covered by net pattern and R_p covered by solid color; c) *I–V* curves tested in electrolysis mode with pure H_2 fed in hydrogen and humidified oxygen (50% H_2O) fed into the oxygen side; d) Total resistance comparison of PNC tested at 1.3 V with R_{ohm} covered by net pattern and R_p covered by a solid color.

demonstrates the high quality of the cell and good sealing. The peak power densities showed the order of PNC73 (0.95 W cm^{-2}) > PNC55 (0.64 W cm^{-2}) > PNC91 (0.59 W cm^{-2}) > PNC37 (0.49 W cm^{-2}) > PNC19 (0.44 W cm^{-2}). Clearly, the PNC73 shows superior fuel cell performance and other electrodes perform 54% (PNC91), 48% (PNC37), 33% (PNC55), and 38% (PNC91) lower peak power densities than PNC73, respectively. The impedance spectra tested under OCV conditions were fitted to an equivalent circuit (Figure S12a, Supporting Information), in which ohmic resistance (R_{ohm}) relates to the total ion transport in the electrolyte, and two parallel RQ circuits associated with R_p from the different electrochemical processes in the electrode. R_{ohm} was obtained by measuring the first intercepts to the *x*-axis (higher frequency range), and the R_p was measured by subtracting the second intercept (lower frequency range) by R_{ohm}. A similar R_{ohm} of the five tested full cells was obtained, indicating the consistent quality of the fabricated half-cells. As shown in Figure 6b, the R_p of the PNC cells was calculated to be 0.38, 0.31, 0.21, 0.11, and 0.22 Ω cm^2 for PNC19, PNC37, PNC55, PNC73, and PNC91, respectively. PNC73 shows the smallest R_p compared to other compositions, which leads to the best fuel cell performance for PNC73 electrode incorporated PCEC.

When the cells were operated in the electrolysis mode, the gas condition was switched to dry hydrogen on the hydrogen-electrode side and humidified oxygen (50% H_2O) on the steam electrode side, respectively. Pure hydrogen was used to avoid the need for gas separation and to help maintain a high OCV of about 0.95 V. From Figure 6c, when PCECs were tested at 1.30 V (slightly higher than the thermoneutral voltage of 1.28 V), the current densities were –1.15, –1.24, –1.37, –1.48, and –1.35 A cm^{-2} for PNC19, PNC37, PNC55, PNC73, and PNC91, respectively. Clearly, PNC73 exhibited greater performance than other compositions in the electrolysis mode. It should be noted that the performance difference under electrolysis mode is much smaller than that in fuel cell mode. This phenomenon was studied by impedance spectra tested at 1.3 V as shown in Figure S12b, Supporting Information. All the impedance spectra under applied current density were distorted, and the respective R_p was reduced dramatically compared to that tested under OCV conditions. PNC73 showed the smallest R_p of 0.019 Ω cm^2 at 1.3 V. For other compositions, PNC19 (0.051 Ω cm^2), PNC37 (0.057 Ω cm^2), PNC55 (0.023 Ω cm^2), and PNC91 (0.037 Ω cm^2) performed 168%, 200%, 21%, and 95% larger R_p than PNC73. Hence, R_p shows less dominance in the overall resistance, as shown in Figure 6d. It is consistent with the results analyzed before in three-electrode symmetric cells that the reduced area-specific resistance (ASR) under an applied electrolysis condition (Figure 2b and Figure S6, Supporting Information), which suggest reducing electrolyte resistance by decreasing thickness, as well as optimizing electrolyte/electrode interface could be two good options for further reducing overall resistance and improving performance in electrolysis working condition.[27] This may be attributed to the enhanced mobility of the charge carriers under the applied overpotential resulting in improved reaction kinetics. Therefore, the fuel cell and electrolysis cell electrochemical performance results from the PCECs with PNC series electrodes suggested that PNC73 with 70% Ni-doped in B-sites has effectively enhanced ORR and WOR activity.

Massachusetts Institute of Technology, after identifying PNC73 as the optimal electrode candidate, more comprehensive electrochemical performance evaluations were carried out to explore its potential of working in PCEC conditions, particularly at lower temperatures. As shown in **Figure 7**a,b, the performance was evaluated at 350–600 °C. In fuel cell mode, the peak power density can reach 0.95, 0.68, 0.45, 0.32, 0.23, and

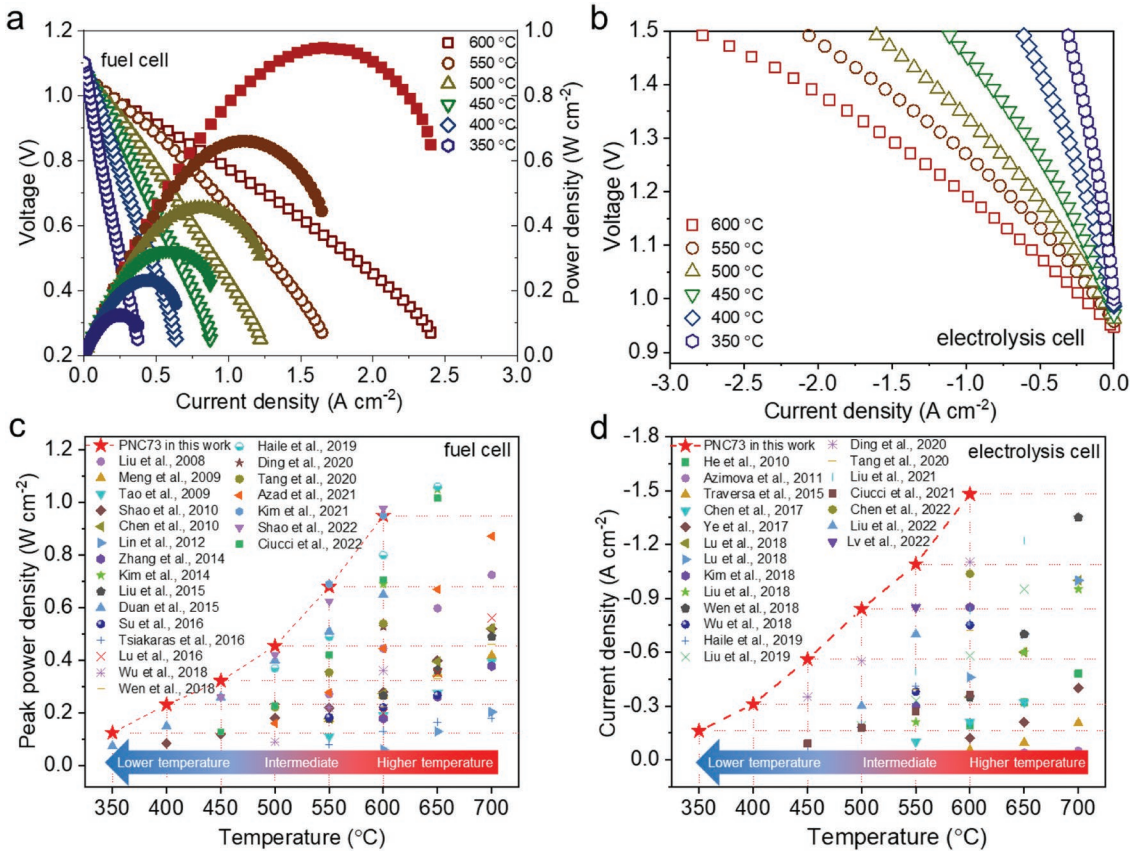

Figure 7. Electrochemical performances of PNC73 series electrodes at temperatures from 350 to 600 °C. a) *I–V* and current–power density (*I–P*) curves in fuel cell mode with wet H_2 (3% steam) fed on the fuel side and pure oxygen fed into the oxygen side; b) *I–V* curve in electrolysis mode with pure H_2 fed in hydrogen and humidified oxygen (50% H_2O) fed into oxygen side; c) Fuel cell mode performance comparison with other PCECs' literature by peak power density at different testing temperature; d) Electrolysis mode performance comparison with other PCECs' literature by electrolysis density testing at 1.3 V and different temperatures.

0.14 W cm^{-2} at 600, 550, 500, 450, 400, and 350 °C, respectively. A PCEC fuel cell operating at 350 °C is the lowest temperature ever reported, emphasizing the possibility for low-temperature operations. Duan et al. have reported a PCEC with complex electrode $BaCe_{0.6}Zr_{0.3}Y_{0.1}O_{3-\delta}$ + $BaCo_{0.4}Fe_{0.4}Zr_{0.1}Y_{0.1}O_{3-\delta}$ that can work at 350 °C. However, the peak power density is relatively low (<0.1 W cm^{-2}).[9] Electrochemical impedance spectra (EIS) of full cells at different temperatures were measured under the OCV condition as shown in Figure S13, Supporting Information. The peak power densities are compared with the literature to demonstrate outstanding performance after adopting this new electrode. As shown in Figure 7c, the power density surpassed many intermediate-temperature cells by a large factor, and the cell demonstrated promising performance in the lower-temperature range.[6,8a,b,9,11,21,28] For example, the performance (0.95 W cm^{-2}) at 600 °C is about 19% and 37% higher than PBSCF (0.8 W cm^{-2})[28m] and $NdBa_{0.5}Sr_{0.5}Co_{1.5}Fe_{0.5}O_{5+\delta}$ (0.69 W cm^{-2}),[8b] respectively.

Figure 7b shows the current–voltage (*I–V*) curves of electrolysis performance in the temperature range of 350–600 °C with humidified oxygen (≈50% H_2O) for the oxygen electrode. At 1.3 V, the electrolysis current density can reach –1.48, –1.09, and –0.84 A cm^{-2} at 600, 550, and 500 °C, respectively. At lower temperatures, the electrolysis current density can still reach –0.56 A cm^{-2} at 450 °C, –0.31 A cm^{-2} at 400 °C, and –0.16 A cm^{-2} at 350 °C, respectively. The superior performance of this cell is among the highest performances of PCECs to date, as shown in Figure 7d.[1b,8a,11,21,28k–m,29] For example, the electrolysis current density of –1.48 A cm^{-2} is more than 100% higher than the 3D self-architectured PBSCF of –0.72 A cm^{-2} when tested at 600 °C and 1.3 V. It is also much higher than triple-conducting R–P structured perovskite $Pr_2NiO_{4+\delta}$ electrode with less than –0.4 A cm^{-2} at the same conditions,[28l] and another R–P oxide $La_{1.2}Sr_{0.8}NiO_4$ which exhibited about –0.42 A cm^{-2}.[21] Our PCEC with PNC73 steam electrode can even deliver almost twice the electrolysis current density than the hybrid electrolysis cells at 600 °C (–0.75 A cm^{-2}) and 550 °C (–0.42 A cm^{-2}) reported by Kim et al.[29g] Therefore, the use of a PNC73 electrode significantly advances the electrochemical performance at intermediate temperatures.

Figure 8 shows the microstructure of a post-tested PCEC integrated with a PNC73 oxygen electrode. The cell remained integral without any observable delamination at the electrode/electrolyte interfaces (Figure 8a). The electrolyte membrane was dense without pinholes or open pores, ensuring no fuel cross-over and good performance. The as-prepared PNC73 shows a stacked branch-like porous structure and adheres to the electrolyte membrane strongly, which can ensure fast gas

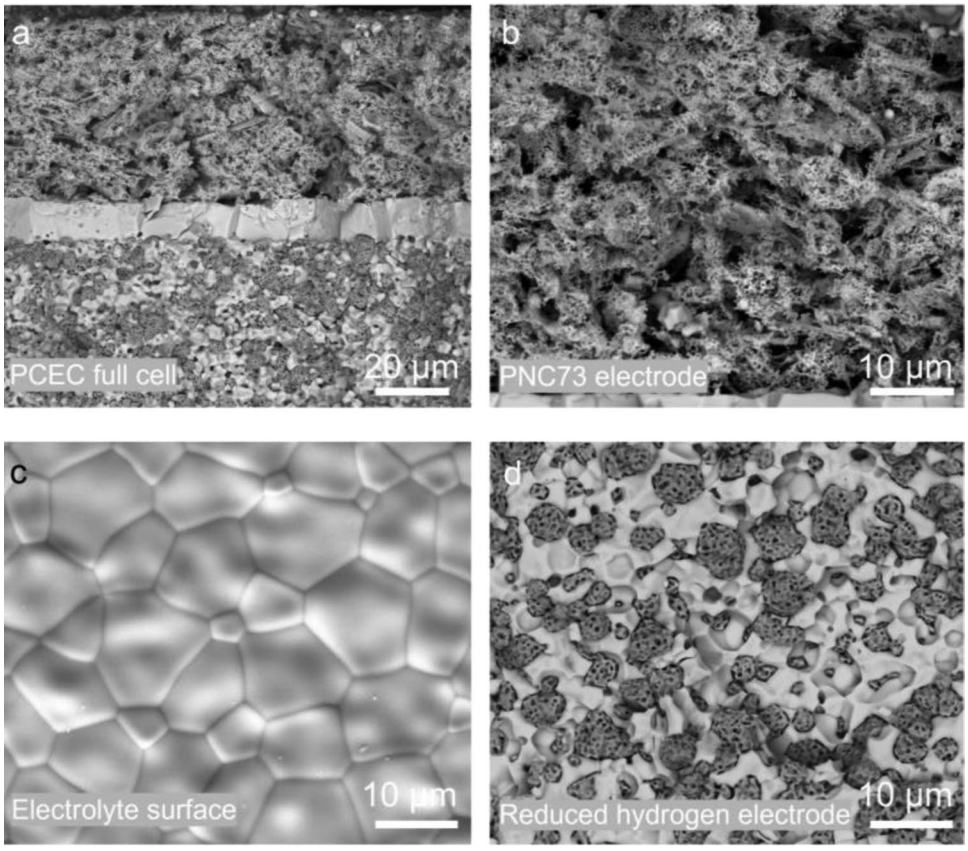

Figure 8. SEM characterization for the post-tested cell with PNC73 electrode. a) Cross-sectional image of the PNC73/BCZYYb4411/NiO-BCZYYb4411 PCEC full cell; b) Porous PNC73 electrode after testing; c) The dense BCZYYb4411 electrolyte membrane surface for the fabricated half cell (before testing); d) The hydrogen electrode with flower-like porous nickel particles after reduction by H_2 in the testing.

diffusion during the reaction (Figure 8b). As a triple-conducting electrode, the porous PNC73 electrode can expand the triple-phase boundary to the entire electrode for promoting the reaction kinetics. The thickness of the electrolyte was measured to be only about 15 μm, which can reduce the ohmic resistance greatly, while grain size on the surface is 8–12 μm (Figure 8c). After testing, the hydrogen electrode shows a flower-like morphology of Ni particles as shown in Figure 8d. These porous Ni particles can facilitate hydrogen gas diffusion and consequently minimize polarization resistance.

In summary, this work presents a new TCO electrode for the PCEC application. The origin of proton conduction in the oxygen electrode PNC oxides has been studied by several surface- and bulk-diffusion characterization techniques and isotope methods to explore the role of the divalent nickel doping level in initiating hydration reaction. The electrochemical performance evaluation fully demonstrated the downselection of the optimal composition of PNC73 electrodes can be favorable for both fuel-cell and electrolysis operations.

3. Conclusion

An oxygen electrode with triple conduction has been successfully developed for PCEC to enable fast hydrogen production and electricity generation. Through a systematic study of the composition by surface/bulk characterizations, isotope exchange, and electrochemical evaluation, the proton conduction in the electrode is confirmed, and the optimal composition of PNC73 is proposed. When the PNC73 electrode is integrated into the electrochemical cell, it demonstrates superior electrolysis and fuel cell performances at intermediate temperature and lower temperature ranges. A high electrolysis current density of –1.48 A cm^{-2} at 1.3 V and a peak power density of 0.95 W cm^{-2} can be achieved at 600 °C in electrolysis mode and fuel cell mode, respectively. This work provides a new strategy to study triple-conducting oxide materials and presents a promising electrode of PNC73 for PCEC application with great potential of being benchmarked for hydrogen production via high steam electrolysis.

4. Experimental Section

Materials Synthesis: PNC series electrode powders were synthesized by the wet-chemistry method as illustrated in Figure S1, Supporting Information. A stoichiometric amounts of $Pr(NO_3)_3\ 6H_2O$ (99.99% purity, Alfa Aesar), $Ni(NO_3)_2\ 6H_2O$ (99.9985% purity, Alfa Aesar), and $Co(NO_3)_2\ 6H_2O$ (99.999% purity, Alfa Aesar) were mixed with glycine and citric acid in deionized water to form a clear precursor solution with cation concentration of ≈0.02 mol L^{-1}. The glycine and citric acid were used as the complexing agent and fuel for the following combustion with a mole ratio of glycine:citric acid:cations = 2:1:1. The precursor

solution was then heated on a hot plate with a magnet stirring. After the water was totally evaporated to form the gel, this was further heated to about 400 °C. Finally, the gel underwent an auto-ignition process, which produced voluminous powder ash. The formed ash was then transferred to a muffle furnace and fired at 1000 °C for 5 h to obtain a crystallized perovskite phase.

$BaCe_{0.4}Zr_{0.4}Y_{0.1}Yb_{0.1}O_{3-\delta}$ electrolyte powder was synthesized by a solid-state reaction method. Stoichiometric amounts of $BaCO_3$ (99.8% purity, Alfa Aesar), ZrO_2 (99.9% purity, Alfa Aesar), CeO_2 (99.9% purity, Alfa Aesar), Y_2O_3 (99.9% purity, Alfa Aesar), and Yb_2O_3 (99.9% purity, Alfa Aesar) were mixed by ball milling at 300 rpm for 12 h in ethanol, followed by drying and calcination at 1400 °C for 12 h in air. The calcined powder was then ball milled (300 rpm for 12 h) and calcinated (1400 °C for 12 h) another time. The final powder was ball milled (350 rpm for 4 h) again before use.

Characterizations: The phase structure of PNC electrodes was determined by XRD (2008 Bruker D8) at room temperature. The morphology and atomic lattice details of the PNC73 powder were characterized by TEM (FEI Tecnai F30). EDX-mapping in TEM was used to analyze the element distribution uniformity. SEAD pattern was characterized to demonstrate the crystal nature. The full cell structure and the post-test cell were examined by an SEM (JEOL 6700F) in backscattering electron mode. Suface chemistry and cation valence of PNC55 and PNC73 were characterized by XPS using a Physical Electronics Versaprobe II X-ray Photoelectron Spectrometer. The digested samples were analyzed for praseodyminm using an ICP-MS (iCAP Q, Thermo Scientific). ICP-OES (iCAP Series 6000, Thermo Scientific) was used to measure cobalt and nickel.

To measure the total electric conductivity, 1 g of PNC powder was pressed with a 4 mm × 20 mm die (Figure S14a, Supporting Information) and then fired at 1250 °C for 5 h to obtain a dense PNC bar (Figure S14b, Supporting Information). As obtained PNC bar was connected to a power supply, a small current was driven through the PNC bar (Figure S14c, Supporting Information). Then the voltage signal was collected with the testing temperature from 200 to 700 °C and the relating bulk conductivity was calculated accordingly.

1 g of BCZYYb4411(1% NiO added) powder was pressed with a 4 mm × 20 mm die and then fired at 1500 °C for 5 h to obtain a dense BCZYYb4411 bar. The thermal expansion of PNC series electrodes and BCZYYb4411 electrolyte dense bars were measured by a dilatometer (DIL 402C, NETZSCH) from room temperature to 1000 °C with a ramping rate of 3 °C min^{-1}.

For the O_2-TPD experiment, first 0.1 g of powder was pre-treated at 500 °C in pure oxygen for 2 h. After cooling down, the dry Ar gas was purged for 1 h to remove the oxygen residues on the surface. Then the desorbed oxygen species were in situ analyzed with mass spectroscopy as the reactor was heated to 700 °C with a ramping rate of 4 °C min^{-1}. For the H_2O-TPD experiment, 0.1 g powder was hydrated at 500 °C in wet Ar (≈3% steam) for 2 h. Similarly, the dry Ar gas was purged for 1 h to remove the steam residues on the surface after cooling down. The desorbed water species were in situ measured by mass spectroscopy while the reactor was heated up to 700 °C with a ramping rate of 4 °C min^{-1}. For the isotope exchange experiment, 0.2 g PNC73 powder was hydrated for 24 h at 200 °C in wet oxygen (≈3% H_2O in O_2). Then the purge gas switched to (≈3%D_2O/97%O_2) to stay for another 24 h for the H/D exchange process. After cooling down to room temperature, dry Ar was used to purge for 1 h to remove the physisorbed D_2O on the surface. Finally, the desorbed water species (H_2O, HDO, and D_2O) were analyzed in situ with mass spectroscopy with a heating rate of 10 °C min^{-1}.

Fabrication of Symmetrical Cells and Full Cells: To prepare the symmetric cells, the BCZYYb4411 electrolyte pellets were first fabricated by uniaxially pressing the powders (BCZYYb4411 + 0.5 wt.% NiO) to form the green pellets for high-temperature sintering at 1500 °C for 5 h to be densified. The PNC electrode slurries were prepared by mixing the electrode powders with binder solution (2% ethyl cellulose in terpineol) and ethanol with ball milling for 10 min. The slurry was then mixed and defoamed to be a thick sticky slurry by a planetary centrifugal mixer (Thinky mixer ARE-310). Symmetrical fuel electrode cells with an active area of 0.494 cm^2 were fabricated by symmetrically printing the slurry on both sides of the electrolyte pellet in the center and calcination at 1000 °C for 3 h.

For the preparation of full cells, the NiO/BCZYYb4411 hydrogen electrode and electrolyte green tapes were first fabricated by the tape casting method. The combined layers of the electrode support and the electrolyte membrane were laminated at 70 °C for 5 h to form the half-cell green tapes. The cells were cut out of the tapes with a diameter of 1.27 cm (0.5 in.) and pre-sintered at 920 °C to remove the organic solvents and binder. Finally, the cells were sintered at 1500 °C for 5 h to densify the electrolyte. Finally, the PNC electrode was fired onto the electrolyte at 1000 °C for 5 h to obtain the final full cells with an active area of 0.178 cm^2.

Electrochemical Performance Measurement: The electrochemical performances of symmetrical cells and PCECs were collected by an electrochemical workstation (Solartron 1400) in a custom testing fixture. For symmetrical cell testing, the ASR of PNC electrodes was measured in wet oxygen (≈3% H_2O) under OCV conditions with a four-probe measurement. The effect of electrolysis current bias on the electrode resistance was studied by measuring impedance at 600 °C when the bias on the PNC73 electrode increased from –10 to –200 mA cm^{-2} in wet oxygen (≈50% H_2O) with the three-electrode measurement method. The electrochemical stability of PNC73 was tested in the same humidity at 600 °C and –100 mA cm^{-2}.

For the full cell testing, the as-fabricated button cell was sealed with a ceramic sealant (Ceramabond 552) onto the testing fixture. Under fuel cell mode testing, the PNC oxygen electrode was exposed to pure oxygen (50 mL min^{-1}), and the fuel electrode was flowing with H_2 with 3% steam (20 mL min^{-1}). After full reduction and a stable OCV was observed at the set temperature, current–voltage curves were collected from 350 to 600 °C. In electrolysis mode testing, the feedstock was pure H_2 for the hydrogen electrode and humidified oxygen (50% steam) for the steam electrode. EIS was measured at OCV (under fuel cell mode) and 1.3 V (under electrolysis mode) with frequency from 10^5 to 0.1 Hz and AC amplitude of 20 mV.

Statistical Analysis: The XRD patterns of PNC series materials were collected from three different batches to confirm the repeatability before application. The electrical conductivity, electrode polarization resistances from symmetric cells, and full cell performances were measured from three different samples with 10% or less standard deviation, and the median values were selected and shown in the resulted figures. Each measurement was repeated at least three times to ensure reliable data collection (<1% error).

Supporting Information

Supporting Information is available from the Wiley Online Library or from the author.

Acknowledgements

This work is supported from the HydroGEN Advanced Water Splitting Materials Consortium, established as part of the Energy Materials Network under the U.S. Department of Energy (USDOE), the Office of Energy Efficiency and Renewable Energy (EERE), the Hydrogen and Fuel Cell Technologies Office (HFTO) under DOE Idaho Operations Office under contract no. DE-AC07-05ID14517, and the Redox seedling project under contract DE-EE0008835. H.L. and M.Z. also would like to acknowledge a subcontract from Idaho National Laboratory as well as funding support from the National Science Foundation (OIA-2119688).

Conflict of Interest

The authors declare no conflict of interest.

Author Contributions

H.D. and D.D. conceived and designed the research. D.D. supervised the entire project. W.T. carried out most of the experiments. W.B., C.V., W.W., W.F., and J.G. characterized or tested samples. W.T., H.D., Y.D., J.L., M.Z., H.L., and D.D. analyzed the data and discussed the results. C.G. and B.B. reviewed the data and discussed the results. W.T. and H.D wrote the paper, and H.L., Y.D., J.L., C.G., B.B., and D.D. reviewed the manuscript. All the authors commented on and revised the manuscript.

Data Availability Statement

The data that support the findings of this study are available from the corresponding author upon reasonable request.

Keywords

oxygen reduction reaction, proton conduction, protonic ceramic electrochemical cells, triple-conducting oxide, water splitting

Received: March 28, 2022
Revised: June 5, 2022
Published online:

[1] a) C. Duan, R. Kee, H. Zhu, N. Sullivan, L. Zhu, L. Bian, D. Jennings, R. O'Hayre, *Nat. Energy* **2019**, *4*, 230; b) W. Li, B. Guan, L. Ma, S. Hu, N. Zhang, X. Liu, *J. Mater. Chem. A* **2018**, *6*, 18057; c) W. Wu, L.-C. Wang, H. Hu, W. Bian, J. Y. Gomez, C. J. Orme, H. Ding, Y. Dong, T. He, J. Li, *ACS Catal.* **2021**, *11*, 12194.

[2] E. Vøllestad, R. Strandbakke, M. Tarach, D. Catalán-Martínez, M.-L. Fontaine, D. Beeaff, D. R. Clark, J. M. Serra, T. Norby, *Nat. Mater.* **2019**, *18*, 752.

[3] a) C. Y. R. Vera, H. Ding, D. Peterson, W. T. Gibbons, M. Zhou, D. Ding, *JPhys. Energy* **2021**, *3*, 032019; b) W. Feng, W. Wu, C. Jin, M. Zhou, W. Bian, W. Tang, J. Y. Gomez, R. Boardman, D. Ding, *J. Power Sources Adv.* **2021**, *11*, 100067; c) Y. Zhou, E. Liu, Y. Chen, Y. Liu, L. Zhang, W. Zhang, Z. Luo, N. Kane, B. Zhao, L. Soule, *ACS Energy Lett.* **2021**, *6*, 1511.

[4] D. Ding, M. Liu, Z. Liu, X. Li, K. Blinn, X. Zhu, M. Liu, *Adv. Energy Mater.* **2013**, *3*, 1149.

[5] W. Bian, W. Wu, C. J. Orme, H. Ding, M. Zhou, D. Ding, *Adv. Funct. Mater.* **2020**, *30*, 1910096.

[6] A. Seong, J. Kim, D. Jeong, S. Sengodan, M. Liu, S. Choi, G. Kim, *Adv. Sci.* **2021**, *8*, 2004099.

[7] S. Choi, C. J. Kucharczyk, Y. Liang, X. Zhang, I. Takeuchi, H.-I. Ji, S. M. Haile, *Nat. Energy* **2018**, *3*, 202.

[8] a) W. Tang, H. Ding, W. Bian, W. Wu, W. Li, X. Liu, J. Y. Gomez, C. Y. R. Vera, M. Zhou, D. Ding, *J. Mater. Chem. A* **2020**, *8*, 14600; b) J. Kim, S. Sengodan, G. Kwon, D. Ding, J. Shin, M. Liu, G. Kim, *ChemSusChem* **2014**, *7*, 2811; c) M. Li, B. Hua, L.-C. Wang, J. D. Sugar, W. Wu, Y. Ding, J. Li, D. Ding, *Nat. Catal.* **2021**, *4*, 274.

[9] C. Duan, J. Tong, M. Shang, S. Nikodemski, M. Sanders, S. Ricote, A. Almansoori, R. O'Hayre, *Science* **2015**, *349*, 1321.

[10] M. Choi, S. J. Kim, W. Lee, *Ceram. Int.* **2021**, *47*, 7790.

[11] H. Ding, W. Wu, C. Jiang, Y. Ding, W. Bian, B. Hu, P. Singh, C. J. Orme, L. Wang, Y. Zhang, D. Ding, *Nat. Commun.* **2020**, *11*, 1.

[12] T. Huang, W. Parrish, H. Toraya, P. Lacorre, J. Torrance, *Mater. Res. Bull.* **1990**, *25*, 1091.

[13] M. Escote, A. Da Silva, J. Matos, R. Jardim, *J. Solid State Chem.* **2000**, *151*, 298.

[14] P. Tomeš, M. Aguirre, R. Robert, A. Shkabko, E. Otal, A. Weidenkaff, *J. Phys. D: Appl. Phys.* **2011**, *44*, 305402.

[15] a) K.-D. Kreuer, *Annu. Rev. Mater. Res.* **2003**, *33*, 333; b) A. Mitsui, M. Miyayama, H. Yanagida, *Solid State Ionics* **1987**, *22*, 213.

[16] A. Løken, S. Ricote, S. Wachowski, *Crystals* **2018**, *8*, 365.

[17] a) W. Bian, W. Wu, Y. Gao, J. Y. Gomez, H. Ding, W. Tang, M. Zhou, D. Ding, *Adv. Funct. Mater.* **2021**, *31*, 2102907; b) R. Ren, Z. Wang, C. Xu, W. Sun, J. Qiao, D. W. Rooney, K. Sun, *J. Mater. Chem. A* **2019**, *7*, 18365.

[18] J. Richter, P. Holtappels, T. Graule, T. Nakamura, L. J. Gauckler, *Monatsh. Chem.* **2009**, *140*, 985.

[19] N. Mahato, A. Banerjee, A. Gupta, S. Omar, K. Balani, *Prog. Mater. Sci.* **2015**, *72*, 141.

[20] L. Liu, R. Guo, C. Wang, C. Zhang, Y. Yang, S. Wang, *J. Solid State Electrochem.* **2014**, *18*, 2771.

[21] S. Yang, Y. Wen, J. Zhang, Y. Lu, X. Ye, Z. Wen, *Electrochim. Acta* **2018**, *267*, 269.

[22] D. Huan, L. Zhang, X. Li, Y. Xie, N. Shi, S. Xue, C. Xia, R. Peng, Y. Lu, *ChemSusChem* **2020**, *13*, 4994.

[23] G. Chen, Y. Luo, W. Sun, H. Liu, Y. Ding, Y. Li, S. Geng, K. Yu, G. Liu, *Int. J. Hydrogen Energy* **2018**, *43*, 12765.

[24] P. Villars, K. Cenzual (Eds). *Springer-Verlag Berlin Heidelberg & Material Phases Data System (MPDS)*, Switzerland & National Institute for Materials Science (NIMS), Japan.

[25] V. Vibhu, A. Flura, C. Nicollet, S. Fourcade, N. Penin, J.-M. Bassat, J.-C. Grenier, A. Rougier, M. Pouchard, *Solid State Sci.* **2018**, *81*, 26.

[26] Y. Yamazaki, F. Blanc, Y. Okuyama, L. Buannic, J. C. Lucio-Vega, C. P. Grey, S. M. Haile, *Nat. Mater.* **2013**, *12*, 647.

[27] W. Bian, W. Wu, B. Wang, W. Tang, M. Zhou, C. Jin, H. Ding, W. Fan, Y. Dong, J. Li, *Nature* **2022**, *604*, 479.

[28] a) L. Yang, C. Zuo, S. Wang, Z. Cheng, M. Liu, *Adv. Mater.* **2008**, *20*, 3280; b) B. Lin, H. Ding, Y. Dong, S. Wang, X. Zhang, D. Fang, G. Meng, *J. Power Sources* **2009**, *186*, 58; c) Z. Tao, L. Bi, Z. Zhu, W. Liu, *J. Power Sources* **2009**, *194*, 801; d) Y. Lin, R. Ran, C. Zhang, R. Cai, Z. Shao, *J. Phys. Chem. A* **2010**, *114*, 3764; e) F. Zhao, S. Wang, K. Brinkman, F. Chen, *J. Power Sources* **2010**, *195*, 5468; f) Y. Ling, X. Yao, X. Zhang, X. Liu, B. Lin, *Int. J. Hydrogen Energy* **2012**, *37*, 5940; g) Z. Tao, G. Hou, N. Xu, X. Chen, Q. Zhang, *Fuel Cells* **2014**, *14*, 135; h) J. Hou, J. Qian, L. Bi, Z. Gong, R. Peng, W. Liu, *J. Mater. Chem. A* **2015**, *3*, 2207; i) L. Fan, P.-C. Su, *J. Power Sources* **2016**, *306*, 369; j) J. Lyagaeva, N. Danilov, G. Vdovin, J. Bu, D. Medvedev, A. Demin, P. Tsiakaras, *J. Mater. Chem. A* **2016**, *4*, 15390; k) D. Huan, N. Shi, L. Zhang, W. Tan, Y. Xie, W. Wang, C. Xia, R. Peng, Y. Lu, *ACS Appl. Mater. Interfaces* **2018**, *10*, 1761; l) W. Wu, H. Ding, Y. Zhang, Y. Ding, P. Katiyar, P. K. Majumdar, T. He, D. Ding, *Adv. Sci.* **2018**, *5*, 1800360; m) S. Choi, T. C. Davenport, S. M. Haile, *Energy Environ. Sci.* **2019**, *12*, 206; n) A. K. Azad, A. M. Abdalla, A. Afif, A. Azad, S. Afroze, A. C. Idris, J.-Y. Park, M. Saqib, N. Radenahmad, S. Hossain, *Sci. Rep.* **2021**, *11*, 19382; o) C. Zhou, X. Shen, D. Liu, J. Cui, Y. Yi, M. Fei, J. Zhou, L. Zhang, R. Ran, M. Xu, *J. Power Sources* **2022**, *530*, 231321; p) Y. Song, J. Chen, M. Yang, M. Xu, D. Liu, M. Liang, Y. Wang, R. Ran, W. Wang, F. Ciucci, *Small* **2022**, *18*, 2200450.

[29] a) F. He, D. Song, R. Peng, G. Meng, S. Yang, *J. Power Sources* **2010**, *195*, 3359; b) M. A. Azimova, S. McIntosh, *Solid State Ionics* **2011**, *203*, 57; c) L. Bi, S. P. Shafi, E. Traversa, *J. Mater. Chem. A* **2015**, *3*, 5815; d) L. Lei, Z. Tao, X. Wang, J. P. Lemmon, F. Chen, *J. Mater. Chem. A* **2017**, *5*, 22945; e) S. Yang, Y. Wen, S. Zhang, S. Gu, Z. Wen, X. Ye, *Int. J. Hydrogen Energy* **2017**, *42*, 28549; f) D. Huan, W. Wang, Y. Xie, N. Shi, Y. Wan, C. Xia, R. Peng, Y. Lu, *J. Mater. Chem. A* **2018**, *6*, 18508; g) J. Kim, A. Jun, O. Gwon, S. Yoo, M. Liu, J. Shin, T.-H. Lim, G. Kim, *Nano Energy* **2018**, *44*, 121; h) W. Li, B. Guan, L. Ma, H. Tian, X. Liu, *ACS Appl. Mater. Interfaces* **2019**, *11*, 18323; i) W. Li, B. Guan, T. Yang, Z. Li, W. Shi, H. Tian, L. Ma, T. L. Kalapos, X. Liu, *J. Power Sources* **2021**, *495*, 229764; j) Y. Song, J. Liu, Y. Wang,

D. Guan, A. Seong, M. Liang, M. J. Robson, X. Xiong, Z. Zhang, G. Kim, *Adv. Energy Mater.* **2021**, *11*, 2101899; k) K. Xu, H. Zhang, Y. Xu, F. He, Y. Zhou, Y. Pan, J. Ma, B. Zhao, W. Yuan, Y. Chen, *Adv. Funct. Mater.* **2022**, *32*, 2110998; l) K. Pei, Y. Zhou, K. Xu, H. Zhang, Y. Ding, B. Zhao, W. Yuan, K. Sasaki, Y. Choi, Y. Chen, *Nat. Commun.* **2022**, *13*, 1; m) Y. Niu, Y. Zhou, W. Zhang, Y. Zhang, C. Evans, Z. Luo, N. Kane, Y. Ding, Y. Chen, X. Guo, *Adv. Energy Mater.* **2022**, *12*, 2103783.

NANO MICRO small

Supporting Information

for *Small,* DOI: 10.1002/smll.202201953

An Unbalanced Battle in Excellence: Revealing Effect of Ni/Co Occupancy on Water Splitting and Oxygen Reduction Reactions in Triple-Conducting Oxides for Protonic Ceramic Electrochemical Cells

Wei Tang, Hanping Ding, Wenjuan Bian, Clarita Y. Regalado Vera, Joshua Y. Gomez, Yanhao Dong, Ju Li, Wei Wu, WeiWei Fan, Meng Zhou, Colin Gore, Bryan M. Blackburn, Hongmei Luo,* and Dong Ding**

Supporting information

Unbalanced Battle in Excellence: Revealing Effect of Ni/Co Occupancy on Water Splitting and Oxygen Reduction Reactions in Triple-Conducting Oxides for Protonic Ceramic Electrochemical Cells

Wei Tang[1,2], Hanping Ding[1,*], Wenjuan Bian[1], Clarita Y. Regalado Vera[1,2], Joshua Y. Gomez[1], Yanhao Dong[3], Ju Li[3], Wei Wu[1], WeiWei Fan[3], Meng Zhou[2], Colin Gore[4], Bryan M. Blackburn[4], Hongmei Luo[2,*], and Dong Ding[1,*]

[1.] Energy and Environment Science & Technology, Idaho National Laboratory, Idaho Falls, ID 83415 USA

[2.] Department of Chemical & Materials Engineering, New Mexico State University, Las Cruces, NM 88003 USA

[3.] Department of Nuclear Science and Engineering and Department of Materials Science and Engineering, Massachusetts Institute of Technology, Cambridge, Massachusetts 02139, USA

[4.] Redox Power Systems, LLC, Beltsville, Maryland 20705, USA

*Corresponding authors. Emails: hanping.ding@inl.gov (H.D.), hluo@nmsu.edu (H.L.), dong.ding@inl.gov (D.D.).

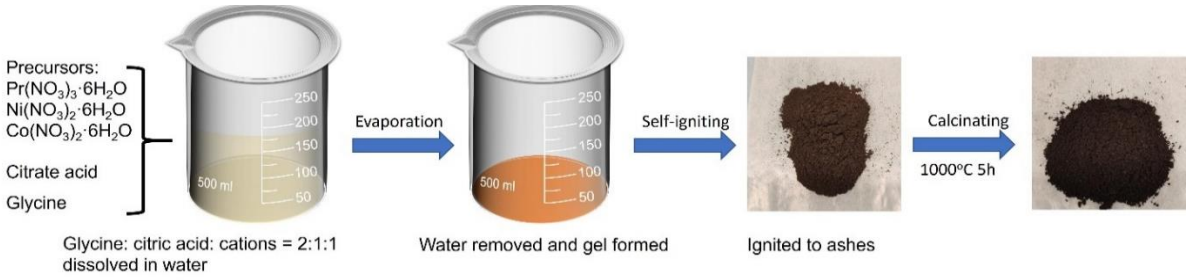

Fig. S1. The illustration of PNC synthesizing procedure by wet-chemistry method.

Table S1. PNC stoichiometry as determined by ICP-AES measurements.

Nominal composition	Corrected composition
$PrNi_{0.1}Co_{0.9}O_{3-\delta}$	$Pr_{1.02}Ni_{0.09}Co_{0.91}O_{3-\delta}$
$PrNi_{0.3}Co_{0.7}O_{3-\delta}$	$Pr_{0.98}Ni_{0.28}Co_{0.73}O_{3-\delta}$
$PrNi_{0.5}Co_{0.5}O_{3-\delta}$	$Pr_{1.02}Ni_{0.48}Co_{0.51}O_{3-\delta}$
$PrNi_{0.7}Co_{0.3}O_{3-\delta}$	$Pr_{0.99}Ni_{0.69}Co_{0.32}O_{3-\delta}$
$PrNi_{0.9}Co_{0.1}O_{3-\delta}$	$Pr_{1.03}Ni_{0.89}Co_{0.10}O_{3-\delta}$

The X-ray photoelectron spectroscopy (XPS) was carried out to measure the chemical status of PNC55 and PNC73 after Ni doping. In general, all cations in PNC55 and PNC73 show mixed valences after Ni doping, and dominant valences are identified after analysis as below:

First, both PNC55 and PNC73 show Pr 3d5/2 and 3d3/2 peaks with at a binding energy of ~ 934 eV and 955 eV, respectively (Figure S2a). Near the Pr 3d5/2 a shake-off satellite (930 eV) was observed which is consistent with previous result.[1] The more intensive peak of Pr 3d5/2 was attributed to Pr^{3+}, indicating +3 is the predominant valence state.[2]

Second, high resolution spectra of Ni 2p was shown in Figure S2b, which consists of the main peak at ~855 eV, shoulder peak at ~858 eV and shake up satellite peak at ~862 eV. Ni 2P3/2 peak at ~855 eV is related to Ni^{2+}, and the relating O 1s peak in +2 valance Ni–O octahedral bonding was located at ~528 eV (Figure S2c).[3] The shoulder peak at ~858 eV and the relating O 1s peak at 531 eV are from the bonding relating to Ni^{3+}.[4] It is noticeable that Ni^{2+} was the main valance in PNC55 and PNC73 materials with the calculated average valance about $Ni^{2.2+}$ for both PNC55 and PNC73, which is similar to the literature.[2]

Third, Figure S2d shows cobalt core-level spectra. The Co^{2+} state does not exist because no peak was observed in the region from 784 to 788 eV in the XPS spectra.[5] Co^{3+} and Co^{4+} were the main valance in both PNC55 and PNC73, and the main peak with binding energies of about 780.2 eV relate to the Co 2p3/2 indicating that Co^{3+} is the main valance status.[6]

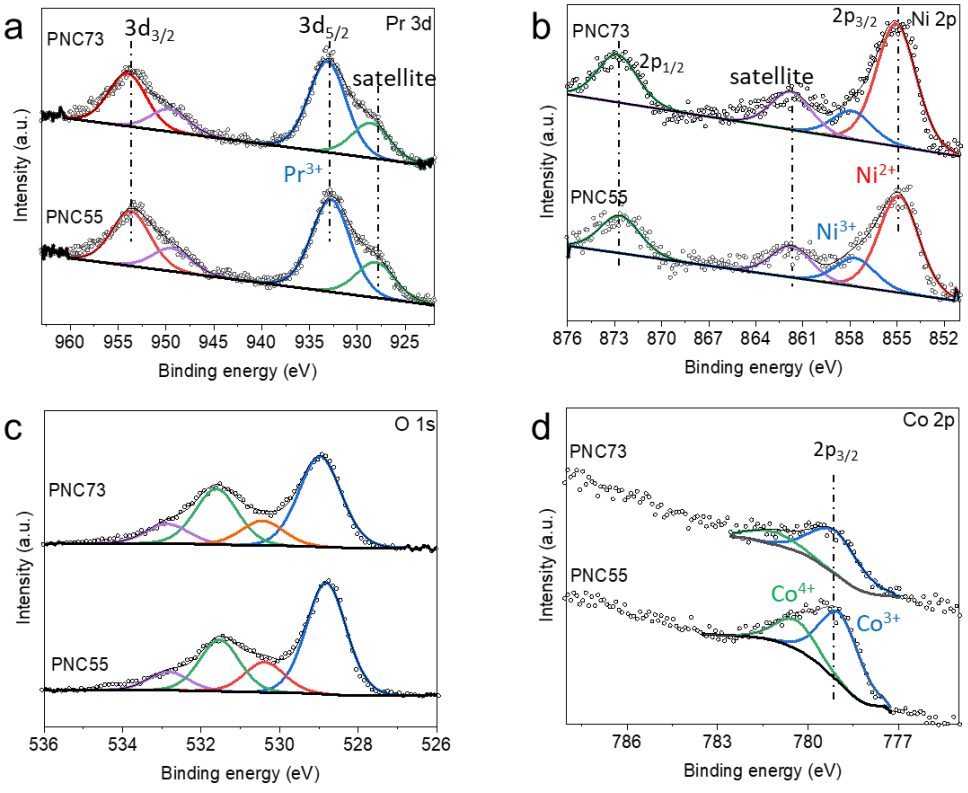

Figure S2. High resolution XPS spectra of PNC55 and PNC73 (a) Pr 3d, (b) Ni 2p, (c) O 1s and (d) Co 2p.

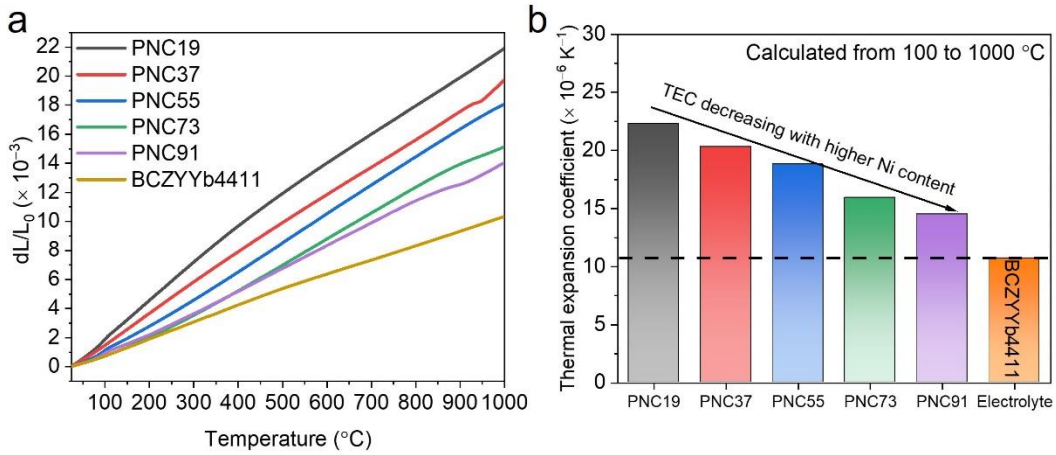

Fig. S3. Thermal-expansion behaviour of PNC series electrode and BCZYYb4411 electrolyte. (a) Thermal-expansion curves of dense PNC and BCZYYb4411 bar specimens from room temperature to 1000 ^{o}C in flowed Ar. (b) Calculated thermal expansion coefficient (TEC) of PNC and BCZYYb4411 bar from 100 to 1000 ^{o}C.

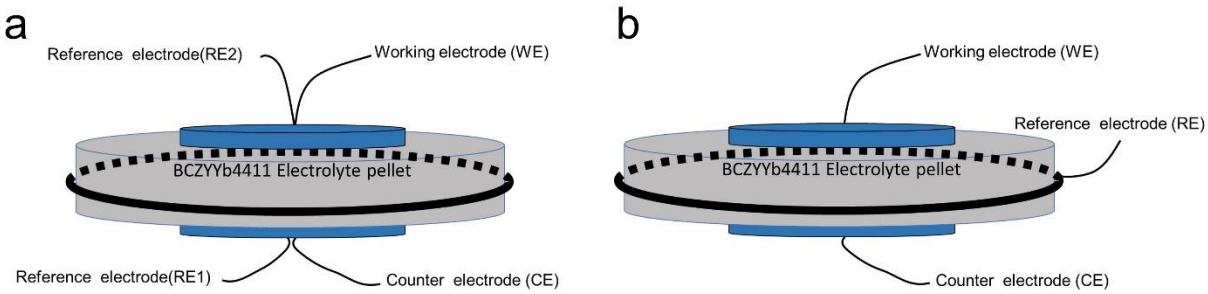

Figure S4. The illustration of symmetrical cell tested with (a) four-probe method and (b) three-electrode method.

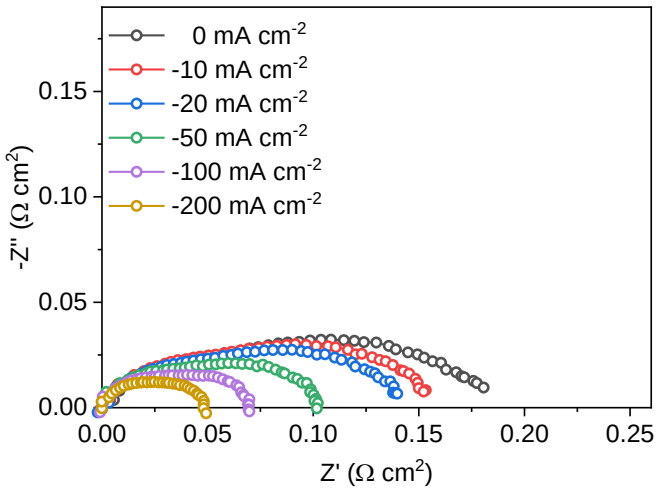

Figure S5. The effect of applied electrolysis current density on the electrode polarization at 600 ^{o}C for the PNC73 electrode tested with the bias current density from −10 to −200 mA cm^{-2}.

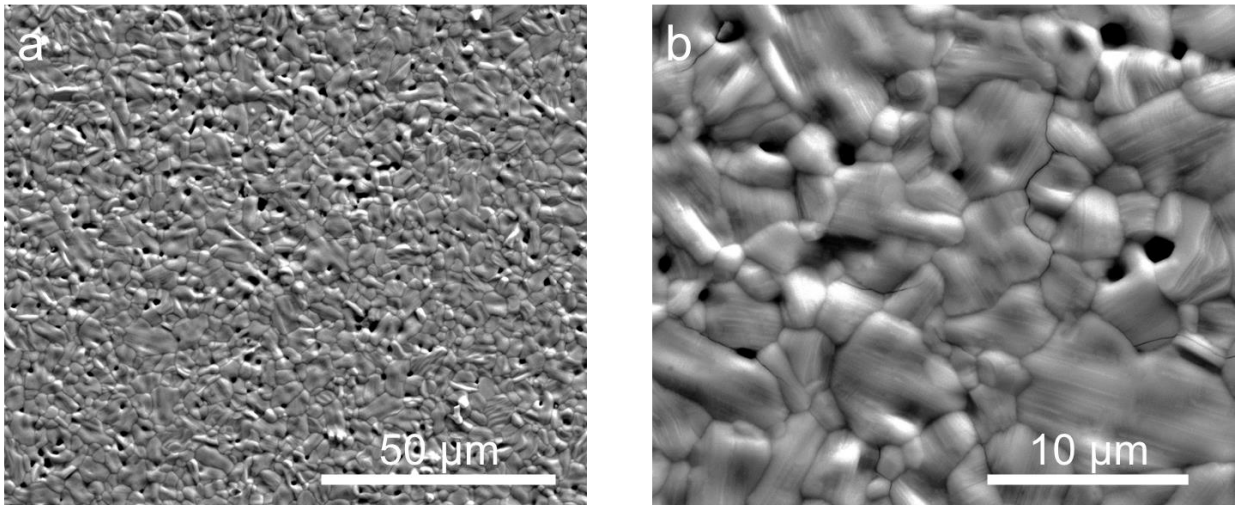

Figure S6. (a) SEM image and (b) magnified SEM image of PNC55 cylinder sintered at 1250C for 5 hours to show the relative dense morphology.

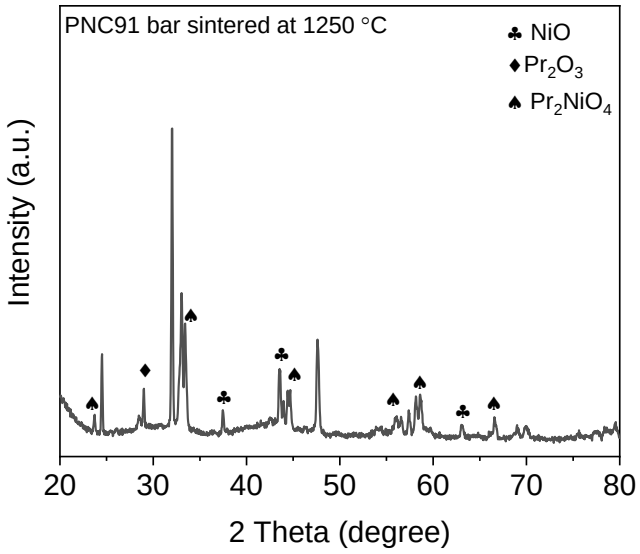

Figure S7. XRD of PNC91 after sintered at 1250 ^{o}C for 5 hours.

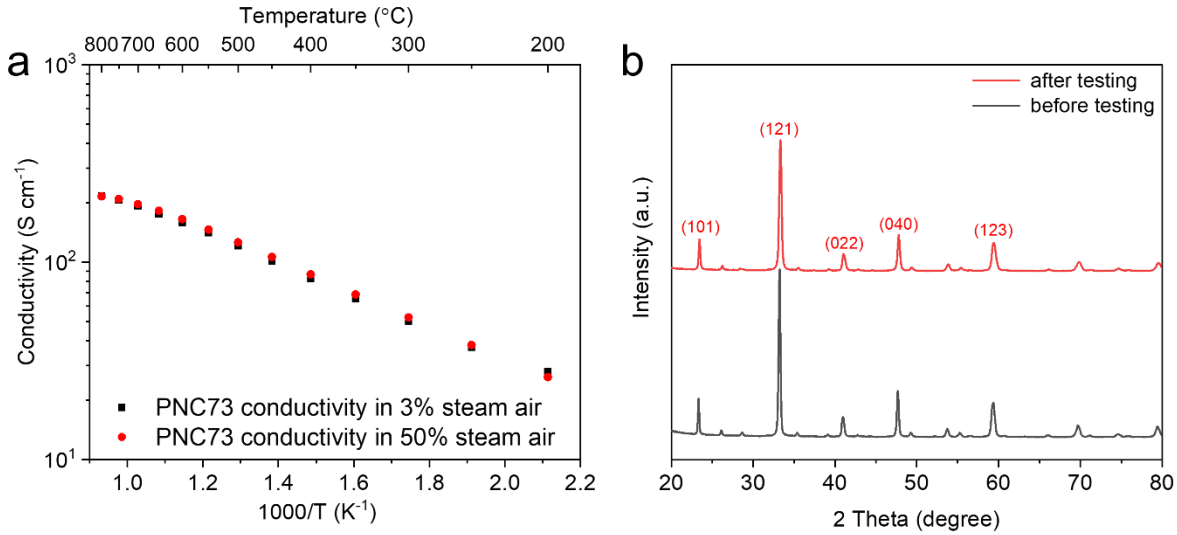

Figure S8. (a) Conductivity measurement of PNC73 at 3% humid air and 50% humid air at temperature ranging from 200 ^{o}C to 800 ^{o}C (b) XRD of PNC73 before and after long-term testing.

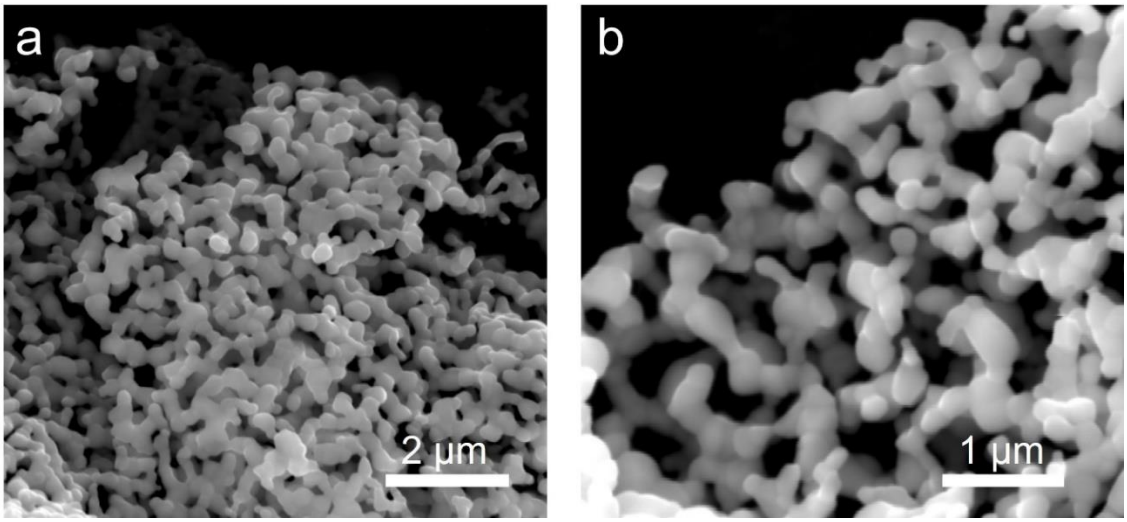

Figure S9. (a) SEM image and (b) magnified SEM image of PNC73 powder

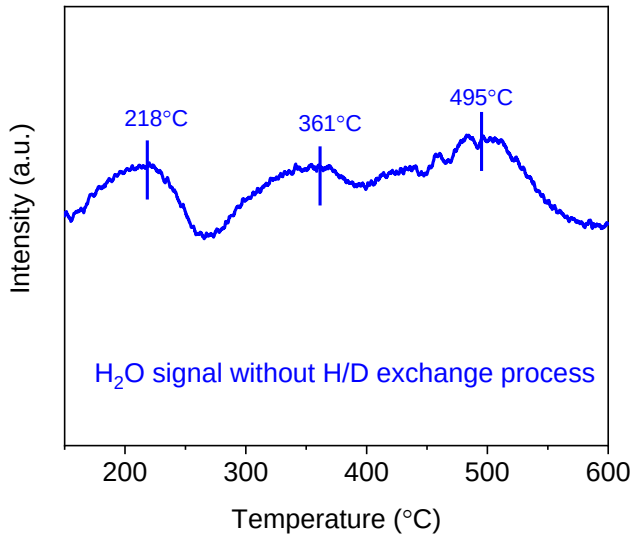

Figure S10. H_2O desorption signal of controlled experiment without isotope exchange process.

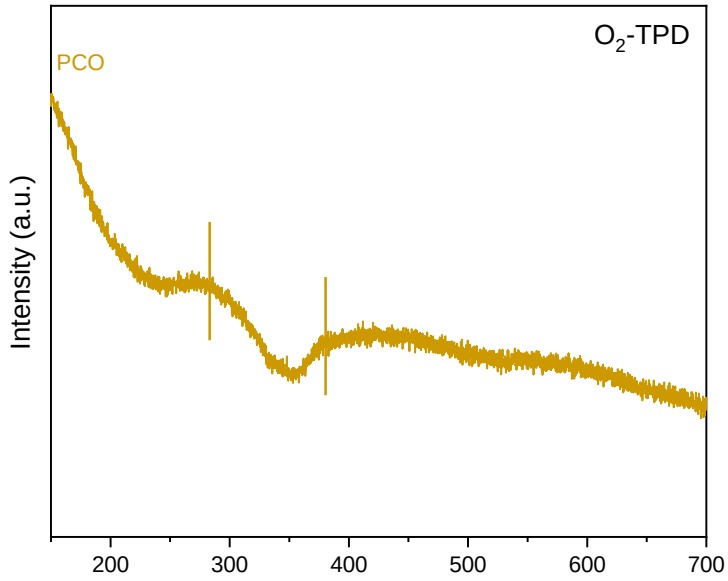

Figure S11. The H_2O-TPD profiles of $PrCoO_3$.

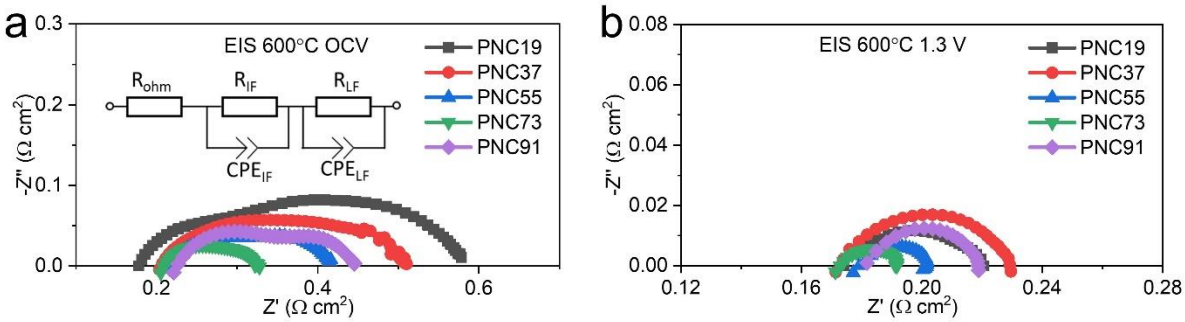

Figure S12. (a) Impedance spectra of PNC series electrode incorporated PCEC tested at 600 ^oC under OCV condition (inset shows equivalent circuit). (b) EIS of PCEC with PNC series electrode tested at 600 ^oC and 1.3 V.

For PNC incorporated full cell, the impedance spectra tested under OCV condition at 600^oC is shown in Figure S8. The inset figure shows the equivalent circuit, in which R_{ohm} relates with the total ion transport in electrolyte, and two parallel RQ circuits associated with polarization resistance from the electrode/electrolyte interface. Figure 8b shows the EIS tested at working voltage of 1.3V. It depicted distorted and reduced R_p compared to the EIS tested under OCV condition. And R_p shows less dominant in the overall resistance at the electrolysis working condition.

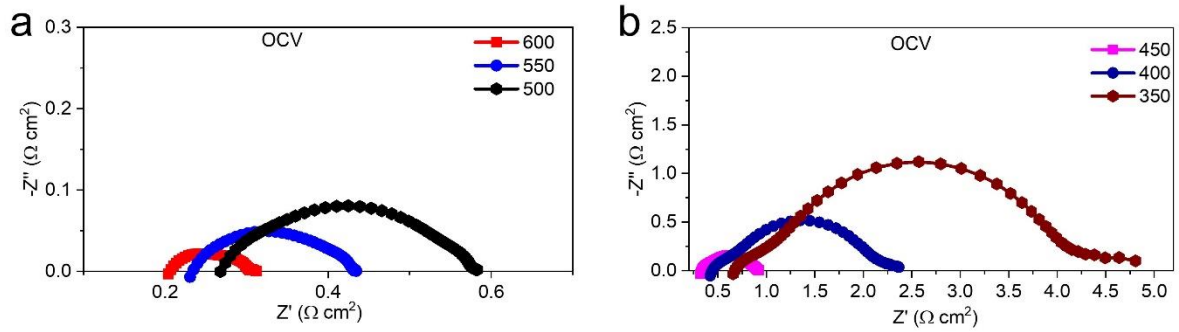

Figure S13. Impedance spectra of PCEC with PNC73 electrode measured under OCV condition with temperature range of (a) 500-600 ^{o}C, and (b) 350-450 ^{o}C.

EIS of PNC73 incorporated full cell at temperature ranging from 350 to 600 ^{o}C was measured under OCV condition shown in Figure S9 a-b. It shows the increased resistance with the decreased temperature, and the R_p gradually take the dominant of the overall resistance when the temperature decreased to 500 ^{o}C and below.

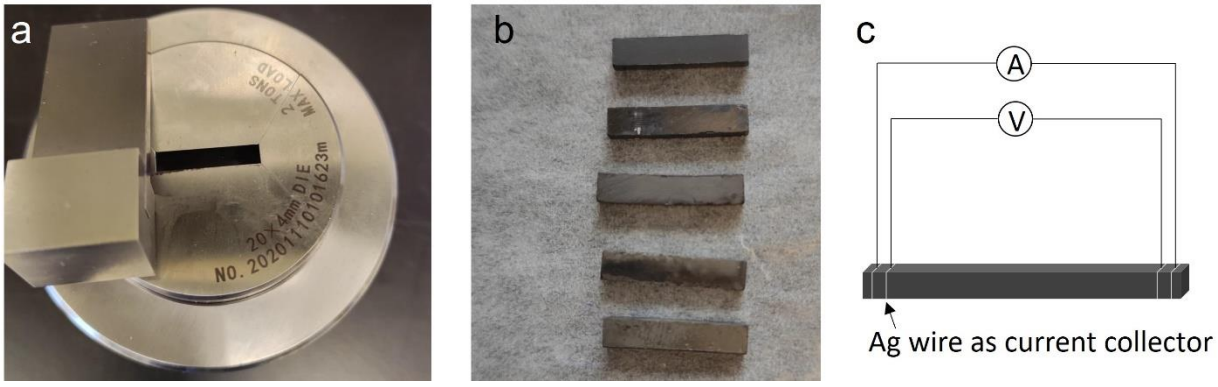

Figure S14. (a) Image of rectangular (20 mm × 4 mm) pressing die, (b) the fabricated PNC dense bar, (c) schematic of total conductivity measurement.

Reference

[1] P. G. Corradini, E. Antolini, J. Perez, *Physical Chemistry Chemical Physics* **2013**, 15, 11730.
[2] P. Tomeš, M. Aguirre, R. Robert, A. Shkabko, E. Otal, A. Weidenkaff, *Journal of Physics D: Applied Physics* **2011**, 44, 305402.
[3] A. Kotta, E.-B. Kim, S. Ameen, H.-S. Shin, H. K. Seo, *Journal of The Electrochemical Society* **2020**, 167, 167517.
[4] U. Kwon, B.-G. Kim, D. C. Nguyen, J.-H. Park, N. Y. Ha, S.-J. Kim, S. H. Ko, S. Lee, D. Lee, H. J. Park, *Scientific reports* **2016**, 6, 1.

[5] S.-J. Huang, A. Muneeb, P. Sabhapathy, A. Sheelam, K. S. Bayikadi, R. Sankar, *Dalton Transactions* **2021**, 50, 7212.
[6] a)X. Xu, C. Su, W. Zhou, Y. Zhu, Y. Chen, Z. Shao, *Advanced Science* **2016**, 3, 1500187; b)M. N. Ha, G. Lu, Z. Liu, L. Wang, Z. Zhao, *Journal of Materials Chemistry A* **2016**, 4, 13155; c)S. K. Singh, P. Kumar, M. Husain, H. Kishan, V. Awana, *Journal of Applied Physics* **2010**, 107, 063905.